


Research Paper

Arcminute-scale studies of the interstellar gas towards HESS J1804–216: Still an unidentified TeV γ -ray source

Kirsty Feijen^{1,*} , Gavin Rowell¹, Sabrina Einecke¹, Catherine Braiding², Michael G. Burton^{2,3}, Nigel Maxted^{4,5}, Fabien Voisin¹ and Graeme F. Wong^{5,6,7}

¹School of Physical Sciences, University of Adelaide, Adelaide, SA 5005, Australia, ²School of Physics, University of New South Wales, Sydney, NSW 2052, Australia, ³Armagh Observatory and Planetarium, College Hill, Armagh BT61 9DG, UK, ⁴School of Science, The University of New South Wales, Australian Defence Force Academy, Canberra, 2600, Australia, ⁵Western Sydney University, Locked Bag 1797, Penrith South DC, NSW 2751, Australia, ⁶Pawsey Supercomputing Centre, 26 Dick Perry Ave, Kensington 6151, WA, Australia and ⁷School of Physics, The University of New South Wales, Sydney 2052, Australia

Abstract

The Galactic TeV γ -ray source HESS J1804–216 is currently an unidentified source. In an attempt to unveil its origin, we present here the most detailed study of interstellar gas using data from the Mopra Southern Galactic Plane CO Survey, 7- and 12-mm wavelength Mopra surveys and Southern Galactic Plane Survey of HI. Several components of atomic and molecular gas are found to overlap HESS J1804–216 at various velocities along the line of sight. The CS(1-0) emission clumps confirm the presence of dense gas. Both correlation and anti-correlation between the gas and TeV γ -ray emission have been identified in various gas tracers, enabling several origin scenarios for the TeV γ -ray emission from HESS J1804–216. For a hadronic scenario, SNR G8.7–0.1 and the progenitor supernova remnant (SNR) of PSR J1803–2137 require cosmic ray (CR) enhancement factors of ~ 50 times the solar neighbour CR flux value to produce the TeV γ -ray emission. Assuming an isotropic diffusion model, CRs from both these SNRs require a slow diffusion coefficient, as found for other TeV SNRs associated with adjacent ISM gas. The morphology of gas located at 3.8 kpc (the dispersion measure distance to PSR J1803–2137) tends to anti-correlate with features of the TeV emission from HESS J1804–216, making the leptonic scenario possible. Both pure hadronic and pure leptonic scenarios thus remain plausible.

Keywords: ISM: clouds – ISM: cosmic rays – ISM: individual objects (HESS J1804–216) – gamma rays: ISM – molecular data

(Received 24 April 2020; revised 4 August 2020; accepted 16 November 2020)

1. Introduction

HESS J1804–216 is one of the brightest unidentified γ -ray sources, discovered by the High Energy Stereoscopic System (H.E.S.S.) in 2004 as part of the first H.E.S.S. Galactic Plane Survey (Aharonian et al. 2005). HESS J1804–216 features extended emission with a radius of ~ 22 arcmin, a photon flux of almost 25% of the Crab Nebula above 200 GeV (Aharonian et al. 2006), and a TeV luminosity of $5 \times 10^{33} (\text{d/kpc})^2 \text{ erg s}^{-1}$ and is one of the softest galactic sources with a photon index of $\Gamma = 2.69 \pm 0.04$ (H.E.S.S. Collaboration et al. 2018a).

High-Altitude Water Cherenkov observatory (HAWC) detected emission at $\sim 4\sigma$ towards the north of HESS J1804–216; however, no source has been identified.

The GeV γ -ray source, FGES J1804.8–2144, (Ackermann et al. 2017) is a disc of radius ~ 23 arcmin, coincident with the TeV emission from HESS J1804–216 (see Figure 1).

HESS J1804–216 has several possible counterparts found within $\sim 1^\circ$ of its centroid, but none of these have been unambiguously associated with the TeV source. Two prominent candidates

for the acceleration of cosmic rays (CRs) are supernova remnants (SNRs) and pulsar wind nebulae (PWNe). Here, the potential counterparts are SNR G8.7–0.1, SNR 8.3–0.1 (also referred to as SNR G8.3–0.0 in other literature, see Hewitt & Yusef-Zadeh 2009), PSR J1803–2137, PSR J1803–2149, and PSR J1806–2125. The location of each counterpart with respect to HESS J1804–216 is shown in Figure 1. The γ -ray contours used here were obtained from Aharonian et al. (2006).

SNR 8.3–0.1 has radio shell-like morphology with a radius of 0.04° (Kilpatrick, Biegging, & Rieke 2016; Acero et al. 2016). Kilpatrick et al. (2016) find a systematic velocity of $+2.6 \text{ km s}^{-1}$, placing it at a kinematic distance of 16.4 kpc, hence it is in the background. SNR 8.3–0.1 would have an unusually high TeV luminosity (H.E.S.S. Collaboration et al. 2018a) at 16.4 kpc of $1.34 \times 10^{36} \text{ erg s}^{-1}$, making it unlikely to be powering HESS J1804–216.

SNR G8.7–0.1 has a large radius of 26 arcmin as determined by radio observations (Fang & Zhang 2008). It has been associated with a number of young HII regions, forming the W30 complex, a large star-forming region with a $\sim 1^\circ$ region of radio continuum emission (Kassim & Weiler 1990). SNR G8.7–0.1 is a mature SNR with an age of 15 kyr (Odegard 1986). A distance of 4.5 kpc is adopted here, which is found through X-ray observations and the column density of neutral hydrogen (Hewitt & Yusef-Zadeh 2009). Ajello et al. (2012) modelled the GeV to TeV emission assuming CRs are accelerated by this SNR.

Author for correspondence: Kirsty Feijen, E-mail: kirsty.feijen@adelaide.edu.au

Cite this article: Feijen K, Rowell G, Einecke S, Braiding C, Burton MG, Maxted N, Voisin F and Wong GF. (2020) Arcminute-scale studies of the interstellar gas towards HESS J1804–216: Still an unidentified TeV γ -ray source. *Publications of the Astronomical Society of Australia* 37, e056, 1–25. <https://doi.org/10.1017/pasa.2020.47>

Table 1. Pulsar characteristics, including spin period (P), period derivative (\dot{P}), characteristic age (τ_c), spin-down power (\dot{E}), distance, and TeV luminosity at that distance.

Pulsar name	P (ms)	\dot{P} (10^{-14})	τ_c (kyr)	\dot{E} (10^{35} erg s $^{-1}$)	Distance (kpc)	TeV luminosity (10^{34} erg s $^{-1}$)
J1803–2137 ^a	133.6	13.41	15.8	22.2	3.8	7.2
J1803–2149 ^b	106.3	1.95	86.4	6.41	1.3	0.8
J1806–2125 ^c	481.8	11.73	65.0	0.41	10	50

^aFrom Brisken et al. (2006).

^bFrom Abdo et al. (2013).

^cFrom Morris et al. (2002).

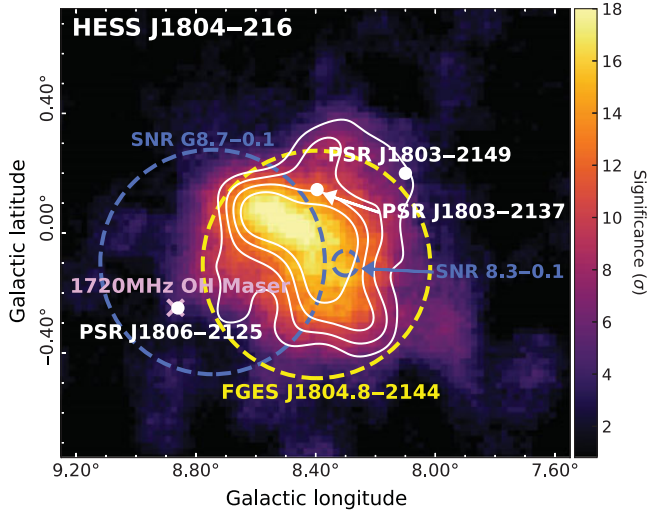


Figure 1. TeV γ -ray significance map of HESS J1804–216, along with potential counterparts. SNR G8.7–0.1 and SNR 8.3–0.1 are indicated by the blue dashed circles, PSR J1803–2137, PSR J1803–2149, and PSR J1806–2125 are indicated by the white dots and the 1720-MHz OH is indicated by a purple cross. FGES J1804.8–2144 is shown by the yellow dashed circle. The TeV γ -ray emission for 5–10 σ is shown by the solid white contours. Image adapted from H.E.S.S. Collaboration et al. (2018a).

A 1720-MHz OH is located along the southern edge of SNR G8.7–0.1 (Hewitt & Yusef-Zadeh 2009). It is currently categorised as an SNR-type maser, as no compact radio source has been found within 5 arcmin and it is believed to originate in a post-shock environment (Fernandez et al. 2013). It is located at a velocity (v_{lsr}) of 36 km s $^{-1}$ corresponding to a distance of ~ 4.55 kpc, similar to the distance to SNR G8.7–0.1. The coexistence of molecular clouds with SNR G8.7–0.1 and the location of the OH maser suggest that the SNR is interacting with nearby molecular clouds (Hewitt & Yusef-Zadeh 2009).

The characteristics of the pulsars are summarised in Table 1. PSR J1803–2137 was found by high-frequency radio observations by Clifton & Lyne (1986). A dispersion measure distance of 3.8 kpc is used here (Kargaltsev, Pavlov, & Garmire 2007a). *Chandra* detected a faint and small (~ 7 arcsec \times 4 arcsec) synchrotron nebula around PSR J1803–2137, with the inner PWN positioned perpendicular to the direction of proper motion of the pulsar (Kargaltsev et al. 2007a).

PSR J1803–2137 is located towards the north-eastern edge of SNR G8.7–0.1, but their association is highly unlikely according to a proper motion study of the pulsar (Brisken et al. 2006). This study showed that for the pulsar to be born at the centre of SNR G8.7–0.1, a transverse velocity of ~ 1700 km s $^{-1}$ is required. Therefore, PSR J1803–2137 was born outside the central

region of SNR G8.7–0.1 (see Figure A1). The pulsar is most likely moving towards this area, rather than away from it, ruling out their connection (Brisken et al. 2006).

PSR J1806–2125 is a γ -ray-quiet radio pulsar discovered with the Parkes radio telescope (Morris et al. 2002), and is located at a distance of ~ 10 kpc. Comparing the inferred γ -ray luminosity at 10 kpc to the spin-down power, we obtain a TeV γ -ray efficiency ($\eta_\gamma = L_\gamma/\dot{E}$) of more than 100%, excluding it as a plausible counterpart.

PSR J1803–2149 is a radio-quiet γ -ray pulsar located at a distance of 1.3 kpc (Pletsch et al. 2012). This distance is obtained by inverting the γ -ray luminosity equation (see Saz Parkinson et al. 2010) and is discussed further in Section 5.1.

Multiple studies (Higashi et al. 2008; Kargaltsev, Pavlov, & Garmire 2007b; Lin, Webb, & Barret 2013) have found a lack of X-ray emission towards HESS J1804–216, particularly towards SNR G8.7–0.1 and PSR J1803–2137. As mentioned previously, there is a faint and small X-ray nebula towards PSR J1803–2137. No SNR shell has been detected within the field of view of the *Chandra* imaging (Kargaltsev et al. 2007b). Investigation of this region by *XMM-Newton* (Lin et al. 2013) showed that the detected X-ray sources (both extended and point-like) are unlikely to be associated with HESS J1804–216 due to them being located far away from the TeV peak.

Our detailed arcminute-scale ISM study here follows on from earlier work by de Wilt et al. (2017) who revealed dense clumpy gas using the ammonia inversion line tracer. By studying the distribution and density of the ISM towards HESS J1804–216 on arcminute scales, we can investigate morphological differences between hadronic and leptonic scenarios for the γ -ray production. We will utilise data from the Mopra radio telescope and Southern Galactic Plane Survey (SGPS) in order to carry out such an investigation and look at an isotropic CR diffusion model for further insight into the likelihood of a hadronic interpretation.

2. ISM observations

In this work, we utilised the publicly available SGPS^a of atomic hydrogen (HI) and 3, 7, and 12 mm (frequency ranges 76–117, 30–50, and 16–27 GHz, respectively) data taken with the Mopra radio telescope towards the HESS J1804–216 region.

The Australia Telescope Compact Array (ATCA) and Parkes telescope together mapped the HI emission along the Galactic Plane to form the SGPS. The survey is for latitudes of $b = \pm 1.5^\circ$ and longitudes covering $l = 253^\circ - 358^\circ$ (SGPS I) as well as $l = 5^\circ - 20^\circ$ (SGPS II, McClure-Griffiths et al. 2005).

Mopra is a single dish with a 22-m diameter surface. The 3-mm data were taken from the Mopra SGPS, which is designed to map the fourth quadrant in the CO isotopologues (e.g. Braiding et al. 2018^b). The Mopra spectrometer (MOPS) was used in wide-band mode at 8 GHz in Fast-On-The-Fly (FOTF) mapping to detect the four isotopologue lines (^{12}CO , ^{13}CO , C^{17}O , and C^{18}O). FOTF mapping is conducted by scanning across 1 square degree segments. To reduce artefacts in the data, each segment contains a longitudinal and latitudinal scan. The target region covering HESS J1804–216 is $b = \pm 0.5^\circ$ and $l = 7.0 - 9.0^\circ$ for the two CO isotopologue lines of interest: ^{12}CO and ^{13}CO .

^aData can be found at https://www.atnf.csiro.au/research/HI/sgps/fits_files.html

^bPublished Mopra data can be found at <https://dataverse.harvard.edu/dataverse/harvard/>

The 7-mm studies towards HESS J1804–216 were taken in 2011 and 2012. The 7-mm coverage is for a 49×52 arcmin region centred on $l = 8.45^\circ$ and $b = -0.07^\circ$. MOPS was used in ‘zoom’ mode for these observations. This provides 16 different subbands each with 4096 channels and a bandwidth of 137.5 MHz (Urquhart et al. 2010). Table F.1 lists the various spectral lines at 7 mm.

The 12-mm receiver on the Mopra telescope was used to carry out the H₂O SGPS (Walsh et al. 2011, HOPS). This survey also detected other molecules such as the different inversion transitions of ammonia (NH₃). HOPS utilised On-The-Fly (OTF) mode with the Mopra wide-bandwidth spectrometer. HOPS mapped the region surrounding HESS J1804–216; $b = \pm 0.5^\circ$ and $l = 7.0^\circ - 9.0^\circ$.

The Mopra 3-, 7-, and 12-mm data must be corrected to account for the extended beam efficiency of Mopra before any data analysis can be performed. The main beam brightness temperature is obtained by dividing the antenna temperature by the extended beam efficiency (η_{XB}). At 3 mm (115 GHz), for the CO(1-0) lines (¹²CO and ¹³CO), a value of $\eta_{XB} = 0.55$ (Ladd et al. 2005) is used. Following Urquhart et al. (2010), the 7-mm data are corrected to account for the beam efficiency of each frequency from Table F.1. At 12 mm for the NH₃(1,1) (24 GHz) line, the main beam efficiency of $\eta_{mb} = 0.6$ is used (Walsh et al. 2011).

The Mopra data were processed using the Australia Telescope National Facility (ATNF) analysis software, LIVE-DATA, GRIDZILLA, and MIRIAD^c. Custom IDL scripts were written to add further corrections and adjustments to the data (see Braiding et al. 2018). LIVEDATA was used first to calibrate each map by the given OFF position and apply a baseline subtraction to the spectra. Next, GRIDZILLA was used to regrid and combine the data from each scan to create three-dimensional cubes (one for each molecular line in Table F.1) of Galactic longitude, Galactic latitude, and velocity along the line of sight (v_{lsr}). The produced FITS file is processed with both MIRIAD and IDL.

3. Spectral line analysis

IDL and MIRIAD were used to create integrated intensity maps. Different parameters, such as the mass and density, are calculated using these integrated intensity maps for each line described within this section. These parameters are examined to calculate important characteristics of each gas component towards HESS J1804–216 (as shown in Sections 5.1 and 5.2).

The mass of each gas region can be calculated, assuming that the gas consists of mostly molecular hydrogen with other constituents of the gas being negligible. The mass relationship is then given by:

$$M = 2m_H N_{H_2} A, \quad (1)$$

where m_H is the mass of a hydrogen atom, N_{H_2} is the mean column density as obtained from each region, and A is the cross-sectional area of the region. The number density of the gas, n , is estimated using the area, A , column density, N_{H_2} , and volume, V of the gas region, $n = N_{H_2} A/V$. For simplicity, we assume a spherical volume for the clouds.

3.1. Carbon monoxide

The focus for the 3-mm study is the $J = 11-0$ transition of the ¹²CO and ¹³CO lines. ¹²CO(1-0) is the standard molecule used to

trace diffuse H₂ gas, as it is abundant and has a critical density of $\sim 10^3 \text{ cm}^{-3}$ (Bolatto, Wolfire, & Leroy 2013). The CO brightness temperature is converted to column density with the use of an X-factor according to Equation (2):

$$N_{H_2} = W_{CO} X_{CO} \text{ cm}^{-2}. \quad (2)$$

Here, N_{H_2} is the column density of H₂, W_{CO} is the integrated intensity of the $J = 1-0$ transition of either ¹²CO or ¹³CO, and X_{CO} is a scaling factor with values presented in Equation (3), from Dame, Hartmann, & Thaddeus (2001) and Simon et al. (2001) for ¹²CO and ¹³CO, respectively:

$$X_{^{12}\text{CO}} = 1.8 \times 10^{20} \text{ cm}^{-2} (\text{K km/s})^{-1},$$

$$X_{^{13}\text{CO}} = 4.92 \times 10^{20} \text{ cm}^{-2} (\text{K km/s})^{-1}. \quad (3)$$

Since the ¹³CO(1-0) line is generally optically thin, as ¹³CO is 50 times less abundant than ¹²CO (Burton et al. 2013), the ¹³CO(1-0) line tends to follow denser regions of gas. The ¹³CO data will provide indication of the dense molecular gas components towards HESS J1804–216.

3.2. Atomic hydrogen

The atomic form of hydrogen is detected through the 21-cm line. The column density corresponding to a specific region is calculated through the relationship $N_{HI} = W_{HI} X_{HI}$. Here, the X-factor is from Dickey & Lockman (1990) (assuming the line is optically thin), as given by Equation (4):

$$X_{HI} = 1.823 \times 10^{18} \text{ cm}^{-2} (\text{K km/s})^{-1}. \quad (4)$$

3.3. Dense gas tracers

As ¹²CO is one of the most abundant molecules in the universe, it quickly becomes optically thick towards dense gas clumps. Tracers of dense gas ($n > 10^4 \text{ cm}^{-3}$) are required to understand the internal dynamics and physical conditions of dense cloud cores. The following paragraphs outline the properties of various molecules used to trace the dense molecular clouds. These have a higher critical density and typically a much lower abundance compared to ¹²CO.

Carbon monosulfide

Carbon monosulfide (CS) is far less abundant (Penzias et al. 1971) than the other molecules previously mentioned and has a much higher critical density, on the order 10^4 cm^{-3} . The average abundance ratio between CS and molecular hydrogen is taken from Frerking et al. (1980) for quiescent gas to be $\sim 10^{-9}$. CS is known to be a good tracer of dense molecular gas, especially in cases where the CO is optically thick. The focus here is CS($J = 1-0$) which is observable with the Mopra 7-mm receiver.

Silicon monoxide

Similar to CS, silicon monoxide (SiO) is a tracer of dense gas and detectable via observing with a 7-mm receiver. The SiO molecule originates in the compressed gas behind a shock moving through the ISM (Martin-Pintado, Bachiller, & Fuente 1992). Such a shock can be found in star formation regions and in SNRs as they interact with the ISM (Gusdorf et al. 2008). SiO can be a useful signpost of disruption in molecular clouds, where the SiO abundance is higher. Nicholas et al. (2012) detected clumps of SiO(1-0) towards various TeV sources, including the W28 SNR.

^c<http://www.atnf.csiro.au/computing/software/>

W28 shows a cluster of 1720-MHz OH masers around the SiO emission, providing evidence of disrupted molecular clouds.

Methanol

Methanol (CH₃OH) emission is a marker for star formation outflows and is an abundant organic molecule in the ISM (Qasim *et al.* 2018). The CH₃OH line is often seen as a Class I maser. The detection of CH₃OH can be indicative of young massive stars and hence star formation regions. CH₃OH has also been detected in SNR shocks, where the gas is heated behind the shock front (Voronkov *et al.* 2010; Nicholas *et al.* 2012).

Cyanopolyynes

A cyanopolyne is a long chain of carbon triple bonds (HC_{2n+1}N) found in the ISM often representing the beginning stages of high-mass star formation. The cyanopolyne used here is cyanoacetylene, HC₃N. HC₃N is typically detected in warm molecular clouds and hot cores. It is present in dense molecular clouds and can be associated with star formation and HII regions (Jackson *et al.* 2013).

Ammonia

The inversion transition of the ammonia molecule is denoted as NH₃(J, K), for different quantum numbers J and K. NH₃ traces the higher density ($n \sim 10^4 \text{ cm}^{-3}$) gas which can be associated with young stars (Ho & Townes 1983; Walsh *et al.* 2011). It is readily observed in dense molecular clouds and towards various HII regions. One common transition is NH₃(1, 1) detected at a line frequency of $\sim 23.69 \text{ GHz}$ (Walsh *et al.* 2011). The spectra of this inversion transition contain the main emission line surrounded by four weaker satellite lines. A study by de Wilt *et al.* (2017) detected NH₃(1, 1) emission towards H₂O masers in the vicinity of HESS J1804–216.

4. Results

The distribution and morphology of interstellar gas along the line of sight of the TeV γ -ray source HESS J1804–216 are investigated in depth within this section. Multiple line emissions are analysed to investigate the characteristics of each ISM gas component along the line of sight. In particular, we are interested in any spatial correlation or anti-correlation between the gas and the TeV γ -ray emission, as mentioned in Section 1.

4.1. Interstellar gas towards HESS J1804–216

A circular region with a radius of 0.42° which encompasses the extent of the TeV γ -ray emission from HESS J1804–216 (shown by the cyan circle in Figure B.1) is used to obtain spectra of the various molecular lines. The emission spectrum of the Mopra CO(1-0) data (Figure 2) shows large regions of gas which overlap with HESS J1804–216 and encompasses the bulk of its emission. Figure C.1 shows a position–velocity (PV) plot of the Mopra ¹²CO(1-0) data, revealing the structure of the gas in velocity space.

The CO(1-0) spectra show a large portion of the emission corresponds to a velocity range of $v_{\text{lsr}} \approx -40$ to 160 km s^{-1} . There are six main regions of emission along the line of sight as denoted by Table 2 and Figure 2. The galactic rotation curve (GRC) model for HESS J1804–216 (Figure D.1) is used to obtain ‘near’ and ‘far’ distances, based on the kinematic velocities to different ISM features.

Table 2. Velocity (v_{lsr}) integration intervals, with the corresponding distance measures, towards HESS J1804–216 based on the components derived from the CO(1-0) spectra in Figure 2.

Component	v_{lsr} (km s^{-1})	Near distance (kpc)	Far distance (kpc)
A	–27 to –10	0.1	17
B	–10 to 8	0.2	16.7
C	8 to 26	3.0	13.8
D	26 to 56	4.9	11.9
E	56 to 105	6.4	10.4
F	105 to 153	7.4	9.5

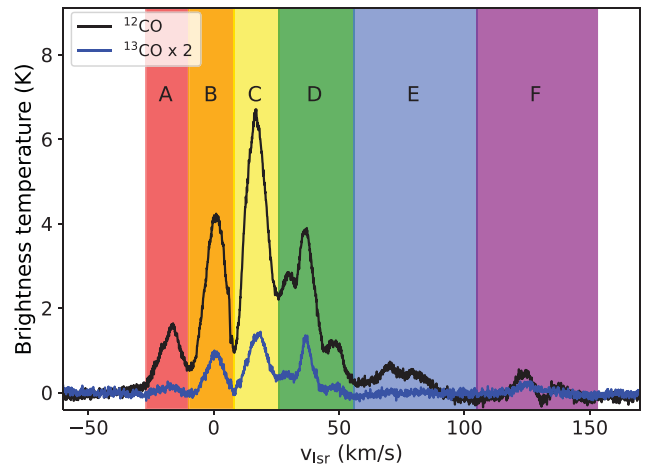


Figure 2. CO(1-0) spectra towards HESS J1804–216 with a radius of 0.42° centred on $[l, b] = [8.4, -0.02]$ (see Figure B.1). Solid black lines and blue lines represent the emission spectra for Mopra ¹²CO(1-0) and ¹³CO(1-0) (scaled by a factor of 2), respectively. Velocity integration intervals for components A through F are shown by the coloured rectangles.

The spectra for the HI data towards HESS J1804–216 exhibit emission and absorption as shown in Figure E.1. Given HI is extremely abundant in the ISM, the data analysis will use the same velocity components as defined above from the CO data (Figure 2).

4.2. Discussion of ISM components

It is important to look at both atomic and molecular hydrogen as they provide a look at the total target material available for CRs. The column density of both ¹²CO and HI are calculated using the X-factors from Equations (2) and (4), respectively. Maps of total column density for the selected integrated velocity ranges are essential in comparing the γ -ray emission and column density for the hadronic scenario. The total hydrogen column density, N_{H} , is the sum of $2N_{\text{H}_2}$ and N_{HI} from Mopra ¹²CO (smoothed up to the beam size of the SGPS HI data) and SGPS HI observations, respectively, giving the total proton content for each gas component. Figure F.5 shows the ratio between the column densities of molecular hydrogen and atomic hydrogen. This figure shows that the molecular gas tends to dominate over the atomic gas. The total column density maps for the defined velocity components are shown in Figure 3. This excludes components E and F (shown in Figure F.4) as these have the weakest emission features and are distant.

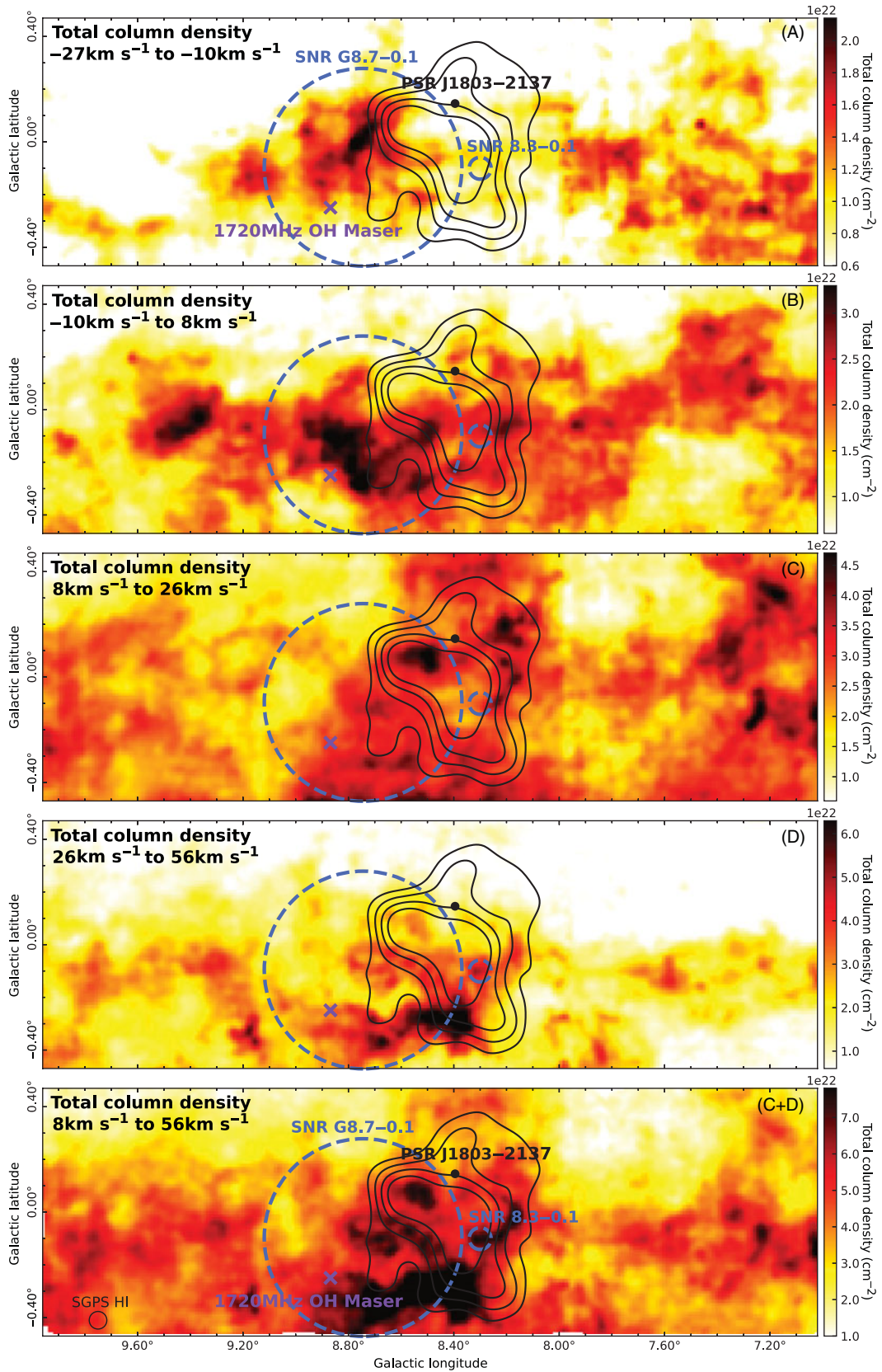


Figure 3. Total column density maps, $2N_{\text{H}_2} + N_{\text{HI}}$, (cm^{-2}) towards HESS J1804–216, for gas components A, B, C, D, and C+D. The two dashed blue circles indicate SNR G8.7 – 0.1 and SNR 8.3–0.1. The 1720-MHz OH is indicated by the purple cross and PSR J1803–2137 is indicated by the black dot. The TeV γ -ray emission for $5\text{-}10\sigma$ is shown by the solid black contours.

Figure 3 also shows an extra component which covers the velocity range $v_{\text{lsr}} = 8$ to 56 km s^{-1} encompassing both components C and D, showing features that overlap much of HESS J1804–216. The dense gas structures in components C and D are connected by a lane of gas as shown in the PV plot (Figures C.1). This indicates that some of the gas in these components are physically close to one another. The distances obtained from the galactic rotation model remain uncertain closer to the Galactic Centre (GC). Due to this, it is possible that the velocity/distance differences in component C and D (see Table 2) arise from local motion.

Figures F.1, F.2, and F.3 show mosaics of the integrated intensity maps of the Mopra $^{12}\text{CO}(1-0)$, $^{13}\text{CO}(1-0)$, and SGPS HI data, respectively. The integrated intensity maps for the dense gas tracers are shown in the Appendix by Figures F.7, F.8, F.9, F.11, and F.11. The CS(1-0) and $\text{NH}_3(1, 1)$ will be discussed here. A number of HII regions seen towards HESS J1804–216 (see Figure B.1) overlap with dense regions of interstellar gas, as discussed here.

4.2.1. Component A

The $^{12}\text{CO}(1-0)$ and $^{13}\text{CO}(1-0)$ emission in component A ($v_{\text{lsr}} = -27$ to -10 km s^{-1}) show little overlap with HESS J1804–216. The emission in this component appears to be localised to the Galactic West of the TeV source.

In HI, there is a gas feature overlapping with the Galactic East edge of SNR G8.7–0.1 which coincides with the central region of HESS J1804–216.

The $\text{NH}_3(1, 1)$ emission towards component A has no distinct features. The CS(1-0) data show two dense features, one in the Galactic North-East of HESS J1804–216 and the other to the Galactic South-East of the TeV source. The Galactic North-East feature overlaps two HII regions, G008.103+00.340 and G008.138+00.228, shown in Figure B.1.

4.2.2. Component B

In component B ($v_{\text{lsr}} = -10$ to 8 km s^{-1}), the $^{12}\text{CO}(1-0)$ emission overlaps most of HESS J1804–216. There is gas filling the inner region of SNR G8.7–0.1, with significant overlap with the Galactic South-West to Galactic West of the TeV source. This emission also extends West beyond both the SNR and TeV source. The $^{13}\text{CO}(1-0)$ emission in this component follows a similar spatial morphology to the $^{12}\text{CO}(1-0)$.

There is no HI overlap with HESS J1804–216 for this component. The HI appears to anti-correlate with the $^{12}\text{CO}(1-0)$ emission.

There is an intense point-like region of $\text{NH}_3(1, 1)$ emission in the central region of SNR G8.7–0.1, which corresponds to a maser detection in both CH_3OH and H_2O (see Figure F.11). CS(1-0) emission in this component is quite weak.

4.2.3. Component C

Component C ($v_{\text{lsr}} = 8$ to 26 km s^{-1}) shows some morphological matches between the $^{12}\text{CO}(1-0)$ emission and the TeV γ -ray emission. There is, however, a depletion in molecular emission slightly south of the centre of HESS J1804–216 (also seen in the $^{13}\text{CO}(1-0)$ emission) which anti-correlates with the southern TeV peak. Additionally, there is a prominent structure of gas running from Galactic East to Galactic West at the bottom of this panel (to the Galactic South of the TeV source). Towards the Galactic West

of HESS J1804–216, there is a molecular cloud which is positionally coincident with the northern edge of SNR G8.7–0.1, as well as another clump of intense emission to the Galactic East of this. Both of these features are also prominent in the $^{13}\text{CO}(1-0)$ emission.

The HI emission (Figure F.3) appears to anti-correlate with the TeV γ -ray emission in component C, with very little emission detected in this area. Two clumps of HI gas overlap with the TeV source to the Galactic North-West and East of SNR 8.3–0.1. In component C, there is also a dense region of gas to the Galactic North-West, the aforementioned clumps are not consistent with the $^{12}\text{CO}(1-0)$ data.

The intense emission towards the Galactic East of PSR J1803–2137 in the total column density map (Figure 3) is also visible in both the CS(1-0) and $\text{NH}_3(1, 1)$ (Figures F.7 and F.11). The significant CS(1-0) emission confirms the presence of dense gas in this region. This dense region is consistent with the infrared (IR) bright clouds and the HII regions G008.103+00.340 and G008.138+00.228, as shown by Figure B.1.

4.2.4. Component D

In component D ($v_{\text{lsr}} = 26$ to 56 km s^{-1}), there is a distinct dense structure in the Galactic South of HESS J1804–216 present in both the $^{12}\text{CO}(1-0)$ and $^{13}\text{CO}(1-0)$ Mopra data. This dense emission overlaps with both SNR G8.7–0.1 and HESS J1804–216, so this region is likely to be associated with the SNR. This feature is consistent with several HII regions: G008.362–00.303, G008.373–00.352, G008.438–00.331, and G008.666–00.351 (as indicated in Figures F.2 and B.1).

There is an intensity gradient in the CO emission as there is less gas towards the Galactic North of this region. The CO emission towards the Galactic North is weak and sparse. There is also weak emission seen outside HESS J1804–216 towards the Galactic West and Galactic East.

The HI emission shows a clear arm-like structure of emission that flows from the Galactic East to Galactic West through HESS J1804–216, most likely corresponding to the Norma Galactic Arm. This overlaps much of the central region of the source.

The $\text{NH}_3(1, 1)$ data for component D show two distinct clumps in the Galactic South which coincide with the previously discussed dense features from the molecular gas. These dense regions overlap with IR emission detected by the Spitzer GLIMPSE Survey in Figure B.1. The IR emission is spatially coincident with several HII regions. The clump outside HESS J1804–216 is also traced by the CS(1-0) emission.

4.2.5. Component E

In component E ($v_{\text{lsr}} = 56$ to 105 km s^{-1}), the $^{12}\text{CO}(1-0)$ overlaps only a small portion of HESS J1804–216, corresponding to the central region of SNR G8.7–0.1. There is a region of intense emission to the Galactic North, near PSR J1803–2137. The $^{13}\text{CO}(1-0)$ emission has less-defined structure with no apparent overlap with the TeV source.

The HI emission appears to have an arm-like structure which extends from the Galactic East to West of HESS J1804–216, with the denser regions towards the Galactic West.

Both the $\text{NH}_3(1, 1)$ and CS(1-0) lines have almost no emission. A dense feature in the Galactic South-West of HESS J1804–216 overlaps the small HII region G008.66–0.00351, shown in Figure B.1.

4.2.6. Component F

Both the $^{12}\text{CO}(1-0)$ and $^{13}\text{CO}(1-0)$ emission in component F ($v_{\text{lsr}} = 105$ to 153 km s^{-1}) show no overlap with the TeV source. This velocity component has little molecular emission aside from the clouds to the Galactic South of HESS J1804–216.

A large HI feature overlaps HESS J1804–216, extending further to the Galactic East in this component.

There is no significant $\text{NH}_3(1, 1)$ emission in component F. In the CS(1-0) data, there is a dense core to the Galactic South-East that has no spatial connection to the TeV γ -ray emission.

5. Discussion

Two different parent particle scenarios will be considered to be producing HESS J1804–216, a purely hadronic scenario and a purely leptonic scenario. As SNRs and PWNe are two candidates for accelerating CRs, the TeV γ -ray emission from HESS J1804–216 could be the result of either scenario as both of these types are present within the field of view. The characteristics (i.e. mass and total column density) of the interstellar gas can be analysed to further investigate the complex nature of emission and to place a limit on which scenario is powering the TeV source.

5.1. Purely hadronic scenario

The hadronic production of TeV γ -rays involves the interaction of CRs and matter in the ISM. A study by Yamazaki et al. (2006) showed that old SNRs tend to have a large enough hadronic contribution to account for the TeV γ -ray emission. This is seen both at the SNR shock location and at the associated molecular clouds.

CRs from SNR G8.7–0.1

Many 1720-MHz OH masers have been seen towards other TeV γ -ray SNRs, such as W28, W44, and IC 443 (Frail, Goss, & Slysh 1994; Claussen et al. 1997), which provides evidence of interaction between the SNR shock and molecular clouds surrounding it (e.g. Nicholas et al. 2012). The presence of the 1720-MHz OH towards SNR G8.7–0.1 is consistent with CRs being accelerated by this SNR. Therefore, this section will assume that SNR G8.7–0.1 is the accelerator of hadronic CRs.

To test whether a hadronic scenario is initially feasible, the total energy budget of CRs, $W_{p,\text{TeV}}$, is calculated using:

$$W_{p,\text{TeV}} = L_{\gamma} \tau_{pp}, \quad (5)$$

where L_{γ} is the luminosity of the γ -ray source. The TeV γ -ray luminosity varies depending on the distance to each counterpart, $L_{\gamma} \sim 5 \times 10^{33} (d/\text{kpc})^2 \text{ erg s}^{-1}$. The cooling time of proton–proton collisions is given by Aharonian & Atoyan (1996):

$$\tau_{pp} = 6 \times 10^7 (n/\text{cm}^{-3})^{-1} \text{ yr}, \quad (6)$$

where n is the number density of the target ambient gas, found in a circular region which encompasses the TeV γ -ray contours of HESS J1804–216 above 5σ , with a radius of 0.42° .

Another relationship can be made between the amount of CRs that are incident upon the gas and the γ -ray flux $F(> E_{\gamma})$ above some energy E_{γ} . The CRs have diffused through the ISM allowing the spectra to steepen from an E^{-2} power law at the accelerator to $E^{-2.6}$ at some distance from the CR source. Therefore, we assume an $E^{-1.6}$ integral power law spectrum from the integration

Table 3. CR enhancement values, k_{CR} (Equation (7)), and total energy budget of CRs, $W_{p,\text{TeV}}$ (Equation (5)), for each velocity component defined in Figure 2. Each of these numbers are calculated from the maximum extent of HESS J1804–216 (circle of radius 0.42°). The values for total mass and column density are obtained from the total column density of hydrogen, using the ^{12}CO and HI data from Mopra and SGPS, respectively. The near distances were derived using the GRC presented in Figure D.1. The magnetic field is calculated using Equation (11).

Component	d (kpc)	n (cm^{-3})	N_{H} (10^{21} cm^{-2})	M ($10^4 M_{\odot}$)	k_{CR}	$W_{p,\text{TeV}}$ (10^{48} erg)	B (μG)
A	0.1	2835	8.6	0.01	123	3×10^{-5}	43
B	0.2	4385	18.8	0.05	56	4×10^{-5}	57
C ^a	3.8	325	29.4	36	57	0.5	11
D ^b	4.5	160	23.7	79	37	1.1	10
C+D	4.4	400	52.9	138	20	0.5	12
E	6.4	25	4.8	27	221	15.8	10
F	7.4	5	1.3	9	842	91.8	10

The values of distance are taken from the kinematic velocity average of each component.

^aComponent C values are taken specifically for PSR J1803–2137.

^bComponent D values are taken specifically for SNR G8.7–0.1.

of $dN_p = E^{-2.6} dE_p$, as given by (Aharonian 1991):

$$F(\geq E_{\gamma}) = 2.85 \times 10^{-13} E_{\text{TeV}}^{-1.6} \left(\frac{M_5}{d_{\text{kpc}}^2} \right) k_{\text{CR}} \text{ cm}^{-2} \text{ s}^{-1}. \quad (7)$$

The photon flux for γ -rays from HESS J1804–216 is $F(\geq 200 \text{ GeV}) = 5.32 \times 10^{-11} \text{ cm}^{-2} \text{ s}^{-1}$ (Aharonian et al. 2006). The distance to the gas component in kpc is d_{kpc} and M_5 is the mass of the CR target material in units $10^5 M_{\odot}$. The CR enhancement factor, k_{CR} , is the ratio of the CR flux at the ISM interaction point compared to that of Earth-like CR flux.

The maps of total column density ($2N_{\text{H}_2} + N_{\text{HI}}$) in Figure 3 were used to find the mean column density of each velocity component in order to calculate both the number densities and masses of each velocity component. Equations 5 and 7 are used to calculate the total CR energy budget ($W_{p,\text{TeV}}$) and the CR enhancement factor (k_{CR}) for each gas component, respectively (shown in Table 3).

An SNR has a total canonical kinetic energy budget of $\sim 10^{51}$ erg, of this we expect an amount of $\sim 10^{50}$ erg ($\sim 10\%$) to be converted into CRs. From Table 3, the total energy budget for components C, D, and C+D are on the order of $W_{p,\text{TeV}} = 10^{48}$ erg which suits the criteria of being $< 10^{50}$ erg. The values of k_{CR} for these ISM components are on the order of ~ 10 , which is acceptable provided we have a young to middle aged (10^3 to 10^5 yrs) impulsive CR accelerator within 10 to 30 pc of the target material (Aharonian & Atoyan 1996).

At a distance of 4.5 kpc, SNR G8.7–0.1 is placed at a kinematic velocity of $\sim 35 \text{ km s}^{-1}$ according to the GRC (outlined in Appendix D). This corresponds to component D as shown in Table 2. The values for total energy budget, $W_{p,\text{TeV}}$, in Table 3 are considered as a lower limit on the total CR energy budget as we are considering γ -rays of energies above 200 GeV corresponding to CR energies of $\sim 1.2 \text{ TeV}$ (from the relation $E_{\gamma} \sim 0.17 E_{\text{CR}}$, in Kelner, Aharonian, & Bugayov 2006). For SNR G8.7–0.1 (component D), we require a CR enhancement factor, k_{CR} , of ~ 37 times that of the Earth-like CR density to produce the observed γ -ray flux towards HESS J1804–216 for a hadronic scenario to be plausible.

The total column density map (Figure 3) shows the ISM partially overlapping the TeV γ -ray emission from HESS J1804–216. This cloud shows a good morphological match with component D (see Figure 3), corresponding to the distance of SNR G8.7–0.1. It is, therefore, possible that this cloud is a target for CRs generated by SNR G8.7–0.1.

Following Aharonian & Atoyan (1996), the volume distribution of CRs ($\text{cm}^{-3} \text{GeV}^{-1}$) as a function of the injection spectrum, $N_0 E^{-\alpha}$, is given by Equation (8). This assumes a spherically symmetric case for the diffusion equation, in which relativistic particles accelerated by a source, escape and enter the ISM:

$$f(E, R, t) \approx \frac{N_0 E^{-\alpha}}{\pi^{3/2} R_{\text{dif}}^3} \exp\left(-\frac{(\alpha-1)t}{\tau_{pp}} - \frac{R^2}{R_{\text{dif}}^2}\right), \quad (8)$$

where the diffusion radius:

$$R_{\text{dif}} \equiv R_{\text{dif}}(E, t) = 2\sqrt{D(E)t \frac{\exp(t\delta/\tau_{pp}) - 1}{t\delta/\tau_{pp}}}, \quad (9)$$

is the radius given for CR protons of energy E propagating through the ISM during time t . The proton–proton cooling time, τ_{pp} , is given by Equation (6) and $\alpha = 2$. We consider a specific CR accelerator model in which the age of SNR G8.7–0.1 is taken to be 15 kyr and 28 kyr from Finley & Oegelman (1994). The diffusion coefficient, $D(E)$, is determined using Equation (10) from Gabici, Aharonian, & Blasi (2007):

$$D(E) = \chi D_0 \left(\frac{E/\text{GeV}}{B/3\mu\text{G}}\right)^\delta, \quad (10)$$

where χ is a diffusion suppression factor (typically $\chi < 1$ inside a molecular cloud). The factor χ from Aharonian & Atoyan (1996) takes values of 0.01 and 1 to represent ‘slow’ and ‘fast’ diffusion, respectively. A value of $\chi = 0.01$ is usually taken to account for the dense regions of interstellar gas that CRs may diffuse through. Various diffusion suppression factors have been found through different studies on the W28 SNR (Li & Chen 2010; Giuliani et al. 2010; Gabici et al. 2010). Li & Chen (2010) assume $\chi = 0.1$, Giuliani et al. (2010) use $\chi = 0.01$, whilst Gabici et al. (2010) adopt a value of $\chi = 0.06$. It is clear that the diffusion suppression factor is poorly constrained. Here, we adopt a value from $\chi = 0.001$ to 0.1. The index of diffusion coefficient, δ , is typically given a value of 0.3–0.7 (Berezinskii et al. 1990). D_0 and δ are given the galactic values of $3 \times 10^{27} \text{cm}^2 \text{s}^{-1}$ and 0.5, respectively, whilst $3 \mu\text{G}$ is the Galactic disc’s average magnetic field. Crutcher et al. (2010) gives a relationship between the magnetic field B and number density n of a given region, shown by Equation (11). They found that the magnetic field is enhanced in dense ($n > 300 \text{cm}^{-3}$) molecular clouds:

$$B = \begin{cases} B_0 & \text{for } n < 300 \text{cm}^{-3} \\ B_0(n/n_0)^{0.65} & \text{for } n > 300 \text{cm}^{-3} \end{cases}, \quad (11)$$

where n is the number density in the cloud, n_0 is a constant number density set to 300cm^{-3} , B is the maximum magnetic field in the cloud, and $B_0 \sim 10 \mu\text{G}$. The various magnetic field values for each ISM component are shown in Table 3.

The normalisation factor, N_0 , is determined assuming the SNR is at an early epoch of evolution ($\sim 1 \text{yr}$) meaning R_{dif} is approximated by the size of the SNR (i.e. $R_{\text{dif}} = R$). The CR energy produced by the SNR is $< 10^{50} \text{erg}$. It is taken here to be $2 \times 10^{48} \text{erg}$ to match the observed GeV and TeV CR enhancement factors as shown in Figure 5. We note that N_0 is considered a lower limit, since the k_{CR} constant from Equation (7) assumes all of the

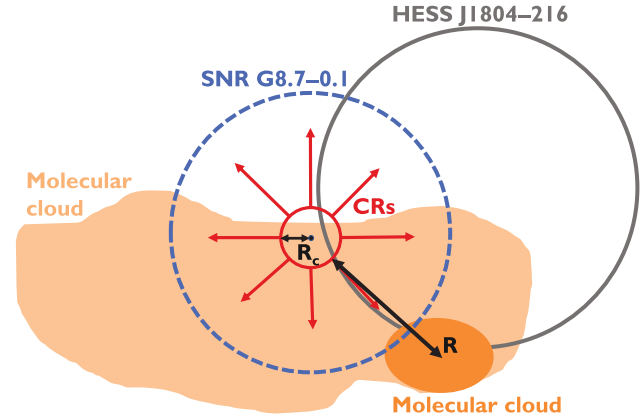


Figure 4. Schematic of CRs escaping SNR G8.7–0.1 before interacting with the molecular clouds in component D to create the TeV γ -ray emission from HESS J1804–216. The red circle shows the release point of CR protons at a radius of $R_c \sim 5 \text{pc}$. The black line shows the physical distance between the cloud and the release point of CRs ($R \sim 12 \text{pc}$).

cloud mass is impacted by CRs and converted to γ -rays. Energy-dependent diffusion and penetration (e.g. Gabici et al. 2007) inside the dense clouds, highlighted by the ^{13}CO peaks in Figure F.2, could however infer a higher k_{CR} value. In addition, clouds are typically not physically connected, given the typically wide range of distances inferred from the cloud velocities spanning Galactic arms (c.f. Figure C.1).

The initial power law distribution is assumed to be $dN/dE = E^{-2}$ for determining N_0 .

The radius of the SNR shock during the Sedov phase (when mass of the swept-up material exceeds the mass of the supernova ejecta) is given by Equation (12) (Reynolds 2008):

$$R_c = 0.31 \left(\frac{E_{51}}{n_0}\right)^{1/5} \left(\frac{\mu_1}{1.4}\right)^{-1/5} t_{\text{yr}}^{2/5} \text{pc}, \quad (12)$$

where E_{51} is the ejected supernova kinetic energy in units of 10^{51}erg , n_0 is the number density, μ_1 is the mean mass per particle (taken to be 1.4, from Reynolds 2008), and t_{yr} is the escape time of CR protons. We assume R_c is the radius at which CR protons are released from the accelerator, which can then be used to calculate the distance to the cloud in component D. For SNR G8.7–0.1, we assume $E_{51} = 1$, with a number density of $n_0 = 160 \text{cm}^{-3}$ for component D. The escape time of CRs (e.g. Gabici, Aharonian, & Casanova 2009) from a SNR shock is

$$t_{\text{esc}} = t_{\text{Sedov}} \left(\frac{E_p}{E_{p,\text{max}}}\right)^{-1/\delta_p}, \quad (13)$$

where the maximum energy of CR protons is $E_{p,\text{max}} = 500 \text{TeV}$, $t_{\text{Sedov}} = 100 \text{yr}$, $E_p = 150 \text{TeV}$, and $\delta_p = 0.5$ (Casanova et al. 2010). Using Equation (12), the release point of the CRs is taken to be $R_c \sim 5 \text{pc}$; therefore, the physical distance to the cloud from this point is $R \sim 12 \text{pc}$. Figure 4 shows a schematic of this scenario where CRs are accelerated by SNR G8.7–0.1 and escape before interacting with the nearby cloud structure defined by component D (Figure 3).

The differential flux of CR protons is then given by:

$$J(E, R, t) = (c/4\pi)f(E, R, t) \text{cm}^{-2} \text{s}^{-1} \text{GeV}^{-1} \text{sr}^{-1}. \quad (14)$$

Figure 5 shows the derived energy spectrum of CR protons escaping from SNR G8.7–0.1 from Equation (8). The scenario

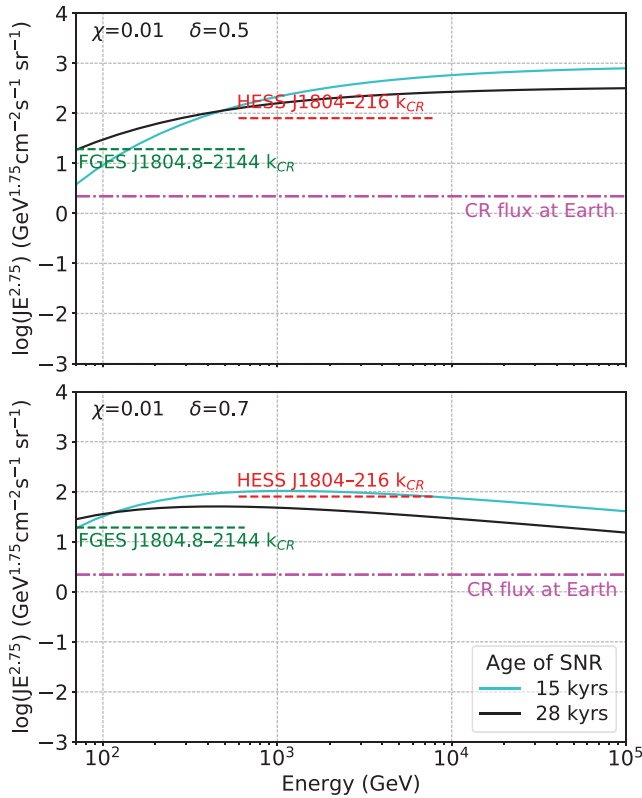


Figure 5. Modelled energy spectra of CR protons (Equation (14)) escaping from a potential impulsive accelerator (e.g. SNR G8.7–0.1), with a total energy of 2×10^{46} erg in CRs. The model shows different values for the diffusion suppression factor, χ , and index of the diffusion coefficient, δ . A power law spectrum with an index of $\alpha = 2$ is assumed. The number density is taken to be $n = 160 \text{ cm}^{-3}$. The distance from the accelerator to the cloud is $R \sim 12 \text{ pc}$ and ages of the source are taken to be 15 kyr and 28 kyr for the cyan and black curves, respectively. The magenta dashed line represents the CR flux observed at Earth. The red dashed line represents the calculated CR enhancement factor for HESS J1804–216 ($k_{\text{CR}} \approx 37$). The green dashed line represents the calculated CR enhancement factor for FGES J1804.8–2144 ($k_{\text{CR}} \approx 9$).

assumes that SNR G8.7–0.1 is an impulsive accelerator meaning the bulk of CRs escape the SNR at $t = 0$, compared to the continuous case in which CRs are continuously injected in the ISM. The CR enhancement factors for component D are shown for TeV energies (from Equation (7) and Table 3) and GeV energies ($k_{\text{CR}} \sim 9$ from Equation (G.1)). Here, we show the two cases that broadly match the observed GeV and TeV CR enhancement factors where δ is 0.5 or 0.7 (Equation (9)) and $\chi = 0.01$. The parameters δ and χ were varied, as shown in Appendix G (Figure G.1), until a reasonable match was found. The contribution from the spectrum of CR protons observed at Earth (i.e. in the solar neighbourhood from Dermer 1986), as given by Equation (15), is also shown:

$$J_{\odot}(E) = 2.2E^{-2.75} \text{ cm}^{-2} \text{ s}^{-1} \text{ GeV}^{-1} \text{ sr}^{-1}. \quad (15)$$

The results in Figure 5 show that the older age assumption for SNR G8.7–0.1 (28 kyr) has a lower energy population of CRs, and the higher energy CRs are seen to escape first, as expected. The total CR energy budget of 2×10^{48} erg is consistent with $W_{p,\text{TeV}}$ from Equation (5) (c.f. Table 3) as computed using component D and tends to match the observed CR enhancement factors. It is evident that the pure hadronic scenario requires slow diffusion ($\chi \leq 0.01$) in order to contribute to the γ -ray emission for

HESS J1804–216. Small values of $\chi < 0.05$ are noted in other studies (Li & Chen 2012; Protheroe et al. 2008; Gabici et al. 2010) for various sources including the W28 SNR, W44, and IC443, all with similar ages to SNR G8.7–0.1. Our diffusion index of δ in the range 0.5 to 0.7 is consistent with Ajello et al. (2012) who found a diffusion index of $\delta = 0.6$ from their modelling of the GeV to TeV emission. We note that the GeV emission position now overlaps the TeV position (Ackermann et al. 2017), whereas previously (in Ajello et al. 2012) the GeV emission was located closer to SNR G8.7–0.1.

In Figure 5, both ages tend to match the CR enhancement factors for HESS J1804–216 and FGES J1804.8–2144.

CRs from the progenitor SNR of PSR J1803–2137

PSR J1803–2137 currently has no known SNR associated with it. Here, we discuss the possibility that the undetected progenitor SNR from PSR J1803–2137 is accelerating CRs. Using the hadronic scenario outlined above, we assume the centre of this SNR is located at the birth position of PSR J1803–2137, placing it in gas component C (consistent with PSR J1803–2137). We assume the progenitor SNR is 16-kyr-old, consistent with the age of PSR J1803–2137. A distance of $\sim 10 \text{ pc}$ is used as the distance from the release point of CRs to the cloud to the Galactic South-West of PSR J1803–2137 in component C. The model in Figure G.2 shows the energy spectrum of CR protons escaping from the progenitor SNR of PSR J1803–2137. The CR enhancement factors for component C are shown for TeV energies ($k_{\text{CR}} \sim 57$) and GeV energies ($k_{\text{CR}} \sim 14$ from Equation (G.1)). A χ value of 0.01 for $\delta = 0.5, 0.7$ or $\chi = 0.001$ for $\delta = 0.7$ could potentially match the observed values from HESS J1804–216 and FGES J1804.8–2144.

5.2. Purely leptonic scenario

PSR J1803–2137 powered PWN

Here, we consider TeV γ -ray emission produced by high-energy (multi-TeV) electrons primarily interacting with soft photon fields via the inverse-Compton process. PSR J1803–2137 is located $\sim 0.2^\circ$ from the centre of HESS J1804–216 (as seen in Figure 1). PSR J1803–2137 is at a distance of 3.8 kpc (see Section 1) which corresponds to a velocity of $\sim 25 \text{ km s}^{-1}$, placing this pulsar in gas component C. Due to the extended nature of HESS J1804–216, and the high spin-down luminosity of PSR J1803–2137, it is possible that the TeV emission is produced by high-energy electrons from PSR J1803–2137 as a PWN. A recent study (H.E.S.S. Collaboration et al. 2018b) shows that 14 firmly identified PWNe contribute to the TeV population of H.E.S.S. sources.

The spin-down luminosity of PSR J1803–2137 ($\dot{E} = 2.2 \times 10^{36} \text{ erg s}^{-1}$) is compared with the γ -ray luminosity of HESS J1804–216 $L_{\gamma} = 7.1 \times 10^{34} \text{ erg s}^{-1}$ at 3.8 kpc to obtain a TeV γ -ray efficiency of $\eta_{\gamma} = L_{\gamma}/\dot{E} \sim 3\%$. This is consistent with the typical efficiency of pulsars (potentially) associated with TeV sources according to H.E.S.S. Collaboration et al. (2018b), meaning leptonic γ -ray emission from a PWN is supported from an energetics point of view.

In the scenario of a PWN-driven TeV γ -ray source, the TeV emission is expected to anti-correlate with the surrounding molecular gas. High-energy electrons suffer significant synchrotron radiation losses due to the enhanced magnetic field strength in molecular clouds, leading to anti-correlation between the gas and γ -rays. Assuming the gas in component C is located at the same

Table 4. Cooling times for synchrotron radiation, t_{sync} (Equation (17)), and Bremsstrahlung, t_{brem} (Equation (18)), towards HESS J1804–216 for each velocity component defined in Figure 2. The diffusion coefficient, $D(E)$, is calculated using Equation (10) with use of the magnetic field strength, B , within each component. The diffusion time, t_{diff} , for particles to cross the 30 pc distance (from PSR J1803–2137 to the nearby cloud in component C), is also shown here.

Component	B (μG)	t_{IC} (kyr)	t_{sync} (kyr)	t_{brem} (kyr)	$D(E)$ ($10^{27} \text{ cm}^2 \text{ s}^{-1}$)	t_{diff} (kyr)
A	43	230	1.3	14	5.6	24
B	57	230	0.73	9	4.9	28
C	11	230	21.6	123	11	12
D	10	230	24.0	253	12	12
E	10	230	24.0	1620	12	12
F	10	230	24.0	7120	12	12

distance as PSR J1803–2137, there is indeed some anti-correlation between the total column density in Figure 3 and the TeV emission towards the Galactic South of the TeV peak.

To account for the observed TeV γ -ray emission, electrons must be able to diffuse across the extent of the GeV and TeV sources. Electrons are therefore required to travel a distance of $R \sim 30$ pc from PSR J1803–2137 to the nearby cloud in component C (see Figure 3). The radiative cooling times are calculated based on the assumption that electrons are being accelerated by PSR J1803–2137.

The inverse-Compton cooling time t_{IC} in the Thomson regime is given by:

$$t_{\text{IC}} \approx 3 \times 10^8 (U_{\text{rad}}/\text{eV}/\text{cm}^3)^{-1} (E_e/\text{GeV})^{-1} \text{ yr}, \quad (16)$$

where U_{rad} is $0.26 \text{ eV}/\text{cm}^3$ (the energy density of the Cosmic Microwave Background). For any given H.E.S.S. source, we expect 100 GeV γ -rays (the lower limit detectable by H.E.S.S.) as produced by inverse-Compton scattering to correspond to electron of energies of $E_e \sim 6 \text{ TeV}$ ($E_e \sim 20\sqrt{E_\gamma}$ for the Thomson scattering regime).

The synchrotron cooling time t_{sync} is given by:

$$t_{\text{sync}} \approx 12 \times 10^6 (B/\mu\text{G})^{-2} (E_e/\text{TeV})^{-1} \text{ yr}, \quad (17)$$

where B is given by Equation (11).

The Bremsstrahlung cooling time t_{brem} is given by:

$$t_{\text{brem}} \approx 4 \times 10^7 (n/\text{cm}^3)^{-1} \text{ yr}, \quad (18)$$

where n is the number density for each given component.

The time, t_{diff} , takes for CRs to diffuse across a given distance, R , is given by:

$$t_{\text{diff}} = R^2/2D(E), \quad (19)$$

where $D(E)$ is the diffusion coefficient (given by Equation (10) for $\chi = 0.1$) for particles of energy, E .

The cooling time for inverse-Compton scattering (t_{IC}) is estimated to be 230 kyr for all ISM components, as it is independent of the ISM density. The various cooling times for the synchrotron and Bremsstrahlung processes, magnetic field (Equation (11)), diffusion coefficient (Equation (10)), and diffusion times (Equation (19)) for each gas component are displayed in Table 4.

Referring to Table 4, component C has a magnetic field value of $B = 11 \mu\text{G}$ and diffusion coefficient of $D(E) = 1.1 \times 10^{28} \text{ cm}^2 \text{ s}^{-1}$, with a corresponding diffusion time of 12 kyr for electrons to cross the TeV source.

As the pulsar's age (16 kyr) is much less than each of the cooling times, the energy losses from each of the cooling effects are negligible at this stage in the pulsar's life. The diffusion time (Equation (19)) for CR electrons of 12 kyr is similar to the age of PSR J1803–2137, suggesting electrons are able to diffuse the required distance of 30 pc in order to contribute to the leptonic TeV emission from HESS J1804–216. Therefore, the leptonic scenario cannot be ruled out and the spatial extent of the emission is limited by diffusion.

PSR J1803–2149 powered PWN

The spin-down power $6.41 \times 10^{35} \text{ erg s}^{-1}$ for PSR J1803–2149 and TeV luminosity of $8.45 \times 10^{33} \text{ erg s}^{-1}$ at 1.3 kpc gives a TeV γ -ray efficiency of 1% for PSR J1803–2149. Therefore, it is possible that PSR J1803–2149 could contribute to the TeV γ -ray emission from HESS J1804–216.

Figure 6 from Abdo *et al.* (2010) shows the population of pulsars with their given γ -ray luminosity L_γ and spin-down power \dot{E} . There is a spread to the data, allowing the authors to place upper ($L_\gamma = \dot{E}$) and lower ($L_\gamma \propto \dot{E}^{1/2}$) bands to this figure. Here, the γ -ray luminosity is given by:

$$L_\gamma \equiv 4\pi d^2 f_\Omega G_{100} \text{ erg s}^{-1}, \quad (20)$$

where f_Ω is the flux correction factor set equal to 1 and $G_{100} = 13.1 \times 10^{-11} \text{ erg cm}^{-2} \text{ s}^{-1}$ is the energy flux obtained from Pletsch *et al.* (2012). Equation (20) can constrain the distance to PSR J1803–2149. The lower and upper limits lead to distances of 1.3 kpc and 6.3 kpc, respectively. As this is within the distances to other counterparts, it is possible that PSR J1803–2149 could be associated with HESS J1804–216. The large angular offset between the TeV peak of HESS J1804–216 and the best-fit position of PSR J1803–2149 of $\sim 0.37^\circ$ indicates that a PWN scenario seems unlikely. More detailed investigation is, however, required to understand if PSR J1803–2149 is a viable counterpart to power the source.

6. Conclusion

In this paper, molecular ISM data from the Mopra radio telescope and HI data from the SGPS were used to study the interstellar gas towards the mysterious unidentified TeV γ -ray source HESS J1804–216. CO(1-0) observations showed different velocity components along the line of sight of HESS J1804–216 which were used to define intriguing features of the interstellar gas along with morphological matches with the TeV γ -ray emission.

The ISM mass and density derived from the total column density maps were used to test the validity of both the purely hadronic and purely leptonic scenarios for the potential CR accelerators towards HESS J1804–216. Components C, D, and C+D were found to contain the bulk of the gas emission towards HESS J1804–216. Component C shows morphological matches between the ^{12}CO and TeV gamma-ray emission. There is also a depletion of gas which anti-correlates with the southern TeV peak. Dense gas emission overlaps both SNR G8.7–0.1 and HESS J1804–216 in component D. The addition of components C and D shows an interesting gas feature which follows the outer most contours of HESS J1804–216 to the south. The southern region of the TeV peak contains a void of gas in this component (C+D).

For the purely hadronic scenario, SNR G8.7–0.1 was assumed to be the accelerator of CRs. Sufficient target material for CRs is

present in component D ($v_{\text{lsr}} = 26$ to 56 km s^{-1}), corresponding to the distance of SNR G8.7–0.1. A total energy budget of $W_{p,\text{TeV}} \sim 1.1 \times 10^{48} \text{ erg}$ for CRs is required, as calculated from the mass of the total target material. For this scenario, we assume CRs have propagated a distance of $R \sim 12 \text{ pc}$ from the accelerator to the cloud, within the lifetime of the SNR. Modelling of the CR spectra showed that the CR interpretation requires slow diffusion ($\chi \leq 0.01$) in order to match the observed GeV and TeV CR enhancement factors. It is, therefore, possible for SNR G8.7–0.1 to generate the TeV γ -ray emission from HESS J1804–216 for the hadronic scenario. We also consider CRs being produced from the undetected progenitor SNR of PSR J1803–2137 for the hadronic scenario. The derived CR enhancement factors for HESS J1804–216 and FGES J1804.8–2144 are well matched for $\chi = 0.01$ or 0.001 .

For the purely leptonic scenario, the TeV emission is produced by highly energetic electrons from PSR J1803–2137 as a PWN. A TeV γ -ray efficiency of $\sim 3\%$ was found, supporting this scenario from an energetics point of view. As the diffusion time for CR electrons of 12 kyr is less than the age of PSR J1803–2137 (16 kyr), the electrons are able to diffuse 30 pc to create a TeV source of this size. Component C (corresponding to the distance of PSR J1803–2137) shows gas structures which anti-correlate with the TeV emission from HESS J1804–216, typical of a PWN-driven TeV source. A PWN from PSR J1803–2137 could, therefore, potentially contribute to the TeV γ -ray emission, so the leptonic scenario cannot be ruled out.

PSR J1803–2149 is also considered for the leptonic scenario. The TeV luminosity at the distance to this pulsar, 1.3 kpc, requires a 1% conversion efficiency of the spin-down power of PSR J1803–2149, a value within the typical efficiencies seen in other firmly identified PWN. However, the large offset between PSR J1803–2149 and the TeV peak of HESS J1804–216 indicates a PWN scenario is unlikely.

HESS J1804–216 still remains unidentified in nature due to the complex environment of the initial detection; however, a middle-aged SNR or PSR provides a valid interpretation. It may also be possible that the TeV emission has contributions from both leptonic and hadronic processes. Future work will focus on modelling the spectral energy distribution in more detail, in particular for the case of high-energy electrons. Future γ -ray observations from the next-generation ground-based observatory, the Cherenkov Telescope Array (CTA), will provide improved angular resolution (few arcminutes) and sensitivity compared to the currently operating telescope arrays. These will provide a more detailed look into many unidentified γ -ray sources, including HESS J1804–216, allowing us to further constrain the nature of HESS J1804–216.

Acknowledgements. The Mopra radio telescope is part of the ATNF which is funded by the Australian Government for operation as a National Facility managed by CSIRO (Commonwealth Scientific and Industrial Research Organisation). Support for observations are provided by the University of New South Wales and the University of Adelaide. This research has made use of the NASA's Astrophysics Data System and the SIMBAD database, operated at CDS, Strasbourg, France. K.F. acknowledges support through the provision of Australian Government Research Training Program Scholarship.

References

Abdo, A. A., et al. 2010, *ApJS*, **187**, 460
 Abdo, A. A., et al. 2013, *ApJS*, **208**, 17
 Acero, F., et al. 2016, *ApJS*, **224**, 8

Ackermann, M., et al. 2017, *ApJ*, **843**, 139
 Ade, P., et al. 2011, *A&A* **536**
 Aharonian, F. A. 1991, *Ap&SS*, **180**, 305
 Aharonian, F. A., & Atoyan A. M. 1996, *A&A*, **309**, 917
 Aharonian, F., et al. 2005, *Science*, **307**, 1938
 Aharonian, F., et al. 2006, *ApJ*, **636**, 777
 Ajello, M., et al. 2012, *ApJ*, **744**, 80
 Anderson, L. D., Bania, T. M., Balsler, D. S., Cunningham, V., Wenger, T. V., Johnstone, B. M., & Armentrout, W. P. 2014a, *VizieR Online Data Catalog*, [p. J/ApJS/212/1](https://vizier.cesr.fr/vizieR/212/1)
 Anderson, L. D., Bania, T. M., Balsler, D. S., et al. 2014b, *APJS*, **212**, 1
 Berezhinskii, V. S., Bulanov, S. V., Dogiel, V. A., & Ptuskin, V. S. 1990, *Astrophysics of cosmic rays*
 Bolatto, A. D., Wolfire, M., & Leroy, A. K. 2013, *ARA&A*, **51**, 207
 Braiding, C., et al. 2018, *PASA*, **35**, e029
 Brand, J., & Blitz, L. 1993, *A&A*, **275**, 67
 Brisken, W. F., Carrillo-Barragán, M., Kurtz, S., & Finley, J. P. 2006, *ApJ*, **652**, 554
 Burton, M. G., et al. 2013, *PASA*, **30**, e044
 Casanova, S., et al. 2010, *PASJ*, **62**, 1127
 Claussen, M. J., Frail, D. A., Goss, W. M., & Gaume, R. A. 1997, *ApJ*, **489**, 143
 Clifton, T. R., & Lyne, A. G. 1986, *Nature*, **320**, 43
 Crutcher, R. M., Wandelt, B., Heiles, C., Falgarone, E., & Troland, T. H. 2010, *ApJ*, **725**, 466
 Dame, T. M., Hartmann, D., & Thaddeus, P. 2001, *ApJ*, **547**, 792
 Dermer, C. D. 1986, *A&A*, **157**, 223
 Dickey, J. M., & Lockman, F. J. 1990, *ARA&A*, **28**, 215
 Fang, J., & Zhang, L. 2008, *MNRAS*, **384**, 1119
 Fernandez, D., et al. 2013, preprint (arXiv:1305.6396)
 Finkbeiner, D. P. 2003, *ApJS*, **146**, 407
 Finley, J. P., & Oegelman, H. 1994, *ApJ*, **434**, L25
 Frail, D. A., Goss, W. M., & Slysh, V. I. 1994, *ApJ*, **424**, L111
 Frerking, M. A., Wilson, R. W., Linke, R. A., & Wannier, P. G. 1980, *ApJ*, **240**, 65
 Gabici, S., Aharonian, F. A., & Blasi, P. 2007, *Ap&SS*, **309**, 365
 Gabici, S., Aharonian, F. A., & Casanova, S. 2009, *MNRAS*, **396**, 1629
 Gabici, S., Casanova, S., Aharonian, F. A., & Rowell, G. 2010, in *SF2A-2010: Proceedings of the Annual meeting of the French Society of Astronomy and Astrophysics*, ed. S. Boissier, M. Heydari-Malayeri, R. Samadi, & D. Valls-Gabaud, 313 (arXiv:1009.5291)
 Giuliani, A., et al. 2010, *A&A*, **516**, L11
 Gusdorf, A., Cabrit, S., Flower, D. R., & Pineau Des Forêts, G. 2008, *A&A*, **482**, 809
 H.E.S.S. Collaboration, et al. 2018a, *A&A*, **612**, A1
 H.E.S.S. Collaboration, et al. 2018b, *A&A*, **612**, A1
 Hewitt, J. W., & Yusef-Zadeh, F. 2009, *ApJ*, **694**, L16
 Higashi, Y., et al. 2008, *ApJ*, **683**, 957
 Ho, P. T. P., & Townes, C. H. 1983, *ARA&A*, **21**, 239
 Jackson, J. M., et al. 2013, *PASA*, **30**, e057
 Kargaltsev, O., Pavlov, G. G., & Garmire, G. P. 2007a, *ApJ*, **660**, 1413
 Kargaltsev, O., Pavlov, G. G., & Garmire, G. P. 2007b, *ApJ*, **670**, 643
 Kassim, N. E., & Weiler, K. W. 1990, *ApJ*, **360**, 184
 Kelner, S. R., Aharonian, F. A., & Bugayov, V. V. 2006, *PhRvD*, **74**, 034018
 Kilpatrick, C. D., Biegging, J. H., & Rieke, G. H. 2016, *ApJ*, **816**, 1
 Ladd, N., Purcell, C., Wong, T., & Robertson, S. 2005, *PASA*, **22**, 62
 Li, H., & Chen, Y. 2010, *MNRAS: Letters*, **409**, L35
 Li, H., & Chen, Y. 2012, *MNRAS*, **421**, 935
 Li, D., et al. 2018, *ApJS*, **235**, 1
 Lin, D., Webb, N. A., & Barret, D. 2013, *ApJ*, **766**, 29
 Martin-Pintado, J., Bachiller, R., & Fuente, A. 1992, *A&A*, **254**, 315
 McClure-Griffiths, N. M., Dickey, J. M., Gaensler, B. M., Green, A. J., Haverkorn, M., & Strasser, S. 2005, *ApJS*, **158**, 178
 Morris, D. J., et al. 2002, *MNRAS*, **335**, 275
 Nicholas, B. P., Rowell, G., Burton, M. G., Walsh, A. J., Fukui, Y., Kawamura, A., & Maxted, N. I. 2012, *MNRAS*, **419**, 251
 Odegard, N. 1986, *AJ*, **92**, 1372

- Penzias, A. A., Solomon, P. M., Wilson, R. W., & Jefferts, K. B. 1971, *ApJ*, **168**, L53
- Planck Collaboration, et al. 2016, *A&A*, **594**, A10
- Pletsch, H. J., et al. 2012, *ApJ*, **744**, 105
- Protheroe, R. J., Ott, J., Ekers, R. D., Jones, D. I., & Crocker, R. M. 2008, *MNRAS*, **390**, 683
- Qasim, D., Chuang, K.-J., Fedoseev, G., Ioppolo, S., Boogert, A. C. A., & Linnartz, H. 2018, *A&A*, **612**, A83
- Reynolds, S. P. 2008, *ARA&A*, **46**, 89
- Saz Parkinson, P. M., et al. 2010, *ApJ*, **725**, 571
- Simon, R., Jackson, J. M., Clemens, D. P., Bania, T. M., & Heyer, M. H. 2001, *ApJ*, **551**, 747
- Sodroski, T. J., Odegard, N., Arendt, R. G., Dwek, E., Weiland, J. L., Hauser, M. G., & Kelsall, T. 1997, *ApJ*, **480**, 173
- Urquhart, J. S., et al. 2010, *PASA*, **27**, 321
- Vallée, J. P. 2014, *AJ*, **148**, 5
- Voronkov, M. A., Caswell, J. L., Ellingsen, S. P., & Sobolev, A. M. 2010, *MNRAS*, **405**, 2471
- Walsh, A. J., et al. 2011, *MNRAS*, **416**, 1764
- Yamazaki, R., Kohri, K., Bamba, A., Yoshida, T., Tsuribe, T., & Takahara, F. 2006, *MNRAS*, **371**, 1975
- de Wilt, P., et al. 2017, *MNRAS*, **468**, 2093

Appendix

A. Pulsar proper motion

The proper motion of PSR J1803–2137 has been studied by Briskin et al. (2006) via radio observations. The proper motion of PSR J1803–2137 has been calculated for the right ascension (RA) and declination (Dec), $\mu_\alpha = (11.6 \pm 1.8) \times 10^{-3}$ arcsec yr⁻¹ and $\mu_\delta = (14.8 \pm 2.3) \times 10^{-3}$ arcsec yr⁻¹, respectively. Given an age of ~ 16 kyr for PSR J1803–2137, a birth position for the pulsar of RA = 18^h03^m38^s.0 and Dec = -21°41'18".2 is obtained, placing it on edge of the W30 SNR, SNR G8.7–0.1.

B. HII regions

HII data were used from the WISE (Anderson et al. 2014b) satellite in order to reveal the known HII regions towards HESS J1804–216 (Figure B.1). These regions were chosen such that their radius was larger than 50 arcmins. The online catalogue (Anderson et al. 2014a) provides the velocity (v_{lsr}) of each HII region, which correspond to kinematic distances ranging from 3 to 5 kpc.

C. PV plot

Figure C.1 is a PV plot towards the HESS J1804–216 region. This figure shows distinct Mopra ¹²CO(1-0) emission in the velocity ranges from $v_{\text{lsr}} = 10$ to 25 km s⁻¹ and $v_{\text{lsr}} = 35$ to 40 km s⁻¹ which is consistent with the molecular gas discussed in Section 4.2.

D. Galactic rotation curve

Objects within the galaxy are rotating around the GC. The GRC is a model which gives the average velocity of an object in the galaxy with respect to the GC as a function of distance. The kinematic distance to an object can be found by knowing the position and radial velocity of the given object, from Equation (D.1) (Brand & Blitz 1993):

$$v_{\text{lsr}} = \left[\frac{\Theta R_0}{R} - \Theta_0 \right] \sin(l) \cos(b) \quad (\text{D.1})$$

where R is the galactocentric distance (distance of an object from the centre of the Milky Way galaxy) to the object and Θ is the circular rotation velocity of object. R_0 is the galactocentric distance from the Sun and Θ_0 is the circular rotation velocity at the position of the Sun, commonly given values 8.5 kpc and 220 km s⁻¹, respectively. The galactic coordinates are given by

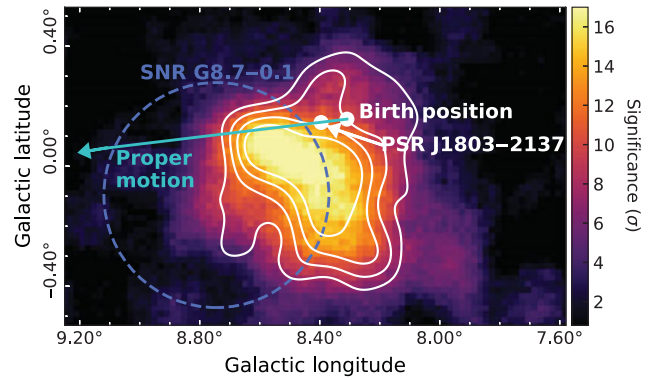


Figure A.1. TeV γ -ray significance image of HESS J1804–216 (H.E.S.S. Collaboration et al. 2018a), showing the proposed proper motion of PSR J1803–2137 (Briskin et al. 2006). The TeV γ -ray emission for 5-10 σ is shown by the solid white contours, SNR G8.7–0.1 is shown by the blue dashed circle, and the white dots indicate PSR J1803–2137 and its birth position.

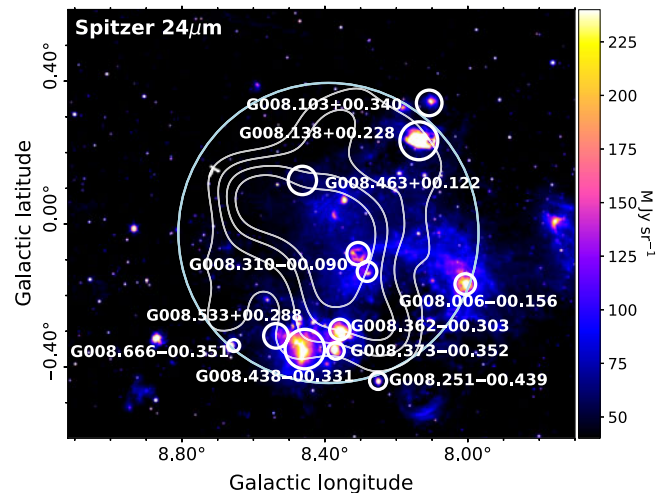


Figure B.1. 24 μm infrared image [M Jy sr^{-1}] towards HESS J1804–216 from the Spitzer GLIMPSE Survey. The TeV γ -ray emission for 5-10 σ is shown by the solid white contours, with the cyan circle showing the extent of HESS J1804–216. HII regions with a radius greater than 50 arcmin are indicated by the white circles from WISE (Anderson et al. 2014b).

l (galactic longitude) and b (galactic latitude). The galactic model along the line of sight for HESS J1804–216 is shown by Figure D.1.

E. HI spectra and absorption

The spectra of the HI data are shown in Figure E.1. Dips tend to occur in the HI spectra which result from either the presence of a background source that leads to absorption or from HI self-absorption. A well-defined HI absorption feature is present at $v_{\text{lsr}} + \sim 20$ km s⁻¹ which corresponds to a strong emission feature in the ¹²CO spectra (shown in Figure 2). This strong absorption feature could be due to a continuum source, such as SNR G8.7–0.1. These properties indicate that the gas is most likely to be foreground to SNR G8.7–0.1. This helps to constrain the distance to the SNR, proving that the pre-defined distance of 4.5 kpc (seen in Section 1) is consistent with the gas data analysis shown here.

F. Integrated intensity maps

The ISM is made up of both atomic and molecular gas, primary HI and ¹²CO emission, respectively. However, there are regions in which these gas tracers become ‘invisible’, due to a lack of emission. It has been shown that

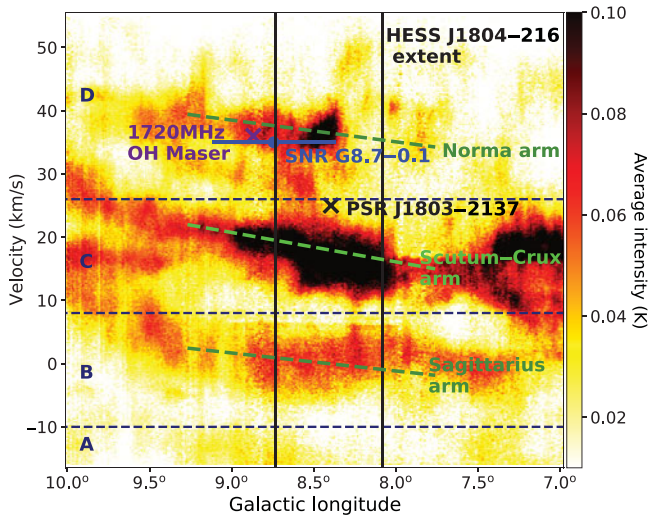


Figure C.1. Position–velocity plot of Mopra $^{12}\text{CO}(1-0)$ emission (K) towards HESS J1804–216. The black vertical lines show the longitudinal extent of HESS J1804–216. The black cross indicates the location of PSR J1803–2137 at its assumed velocity of $\sim 25 \text{ km s}^{-1}$. The 1720-MHz OH maser is shown by the purple cross at its velocity of 36 km s^{-1} . The centre of SNR G8.7–0.1 is shown by the blue dot, whilst the blue line shows its radial extent. The green dashed lines are estimates of the Galactic spiral arms along the line of sight for HESS J1804–216 (from the model in Vallée 2014).

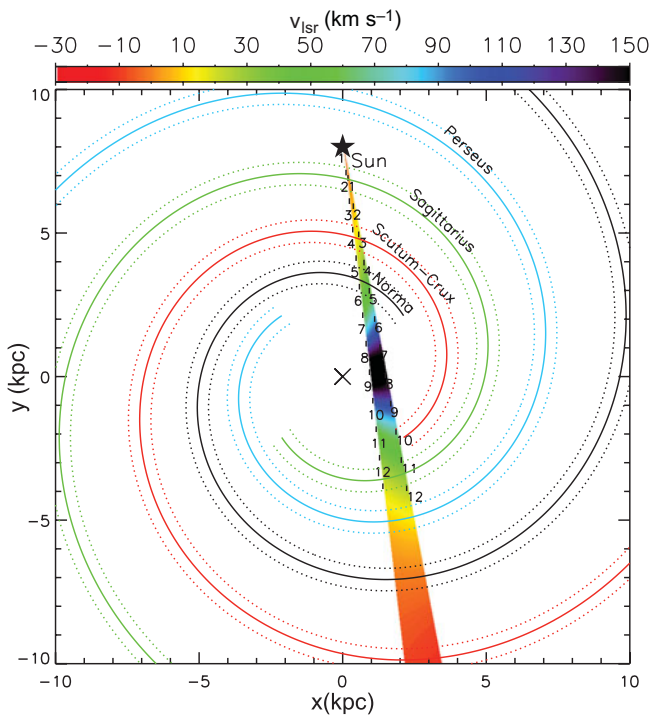


Figure D.1. Model of the galaxy along the line of sight of HESS J1804–216. Parameters used in this model are from Vallée (2014) for each spiral arm shown by the solid coloured lines, Perseus (light blue), Sagittarius (light green), Scutum–Crux (red), and Norma (black). The dashed lines for each spiral arm show their extent. The coloured wedge shows the expected line of sight for HESS J1804–216 from the Sun for the radial velocities (v_{lsr}) using the galactic rotation model from Brand & Blitz (1993). The numbers along this wedge show the distance to the source in kiloparsecs (kpc). The spatial coordinates along the axes are given in kpc also.

Table F.1 Molecular lines with each of their rest line frequencies from the 7-mm receiver of the Mopra telescope.

Molecular line	Line rest frequency (GHz)
$^{30}\text{SiO}(1-0, v = 0)$	42.373365
$\text{SiO}(1-0, v = 3)$	42.519373
$\text{SiO}(1-0, v = 2)$	42.820582
$\text{SiO}(1-0, v = 1)$	43.122079
$\text{SiO}(1-0, v = 0)$	43.423864
$\text{CH}_3\text{OH}(1)$	44.069476
$\text{HC}_7\text{N}(40-39)$	45.119064
$\text{HC}_5\text{N}(17-16)$	45.264750
$\text{HC}_3\text{N}(5-4, F = 5-5)$	45.488839
$^{13}\text{CS}(1-0)$	46.247580
$\text{HC}_5\text{N}(16-15)$	47.927275
$\text{C}^{34}\text{S}(1-0)$	48.206946
$\text{OCS}(4-3)$	48.651604
$\text{CS}(1-0)$	48.990957

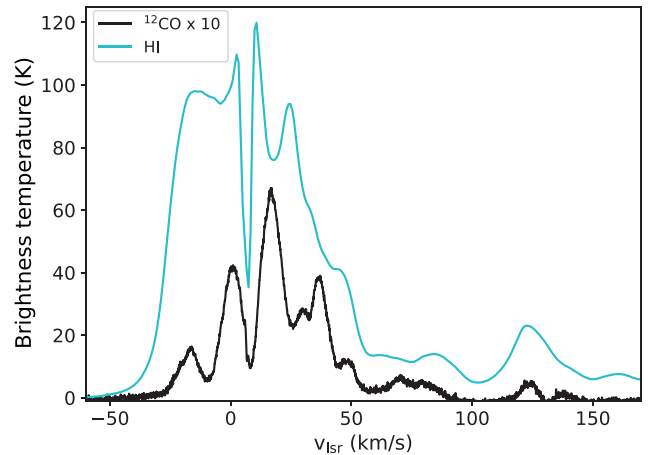


Figure E.1. Emission spectrum towards HESS J1804–216. Solid black lines and cyan lines represent the spectrum for Mopra $^{12}\text{CO}(1-0)$ and SGPS HI, respectively. ^{12}CO is scaled by a factor of 10 for clarity.

there is a component of gas which has not been detected, commonly known as ‘dark’ gas (Li et al. 2018).

In addition to the common neutral gas tracers (HI and ^{12}CO), a component of ionised gas is present in interstellar clouds. For cases in which clouds are optically thick, the dust opacity that maps from the Planck collaboration (Planck Collaboration et al. 2016) can be used to estimate a hydrogen column density (Ade et al. 2011). The column density derived via this method contains no distance information as the dust opacity map has been summed over the line of sight. The Planck hydrogen column density is, therefore, an upper limit.

To determine the Planck HII column density, the free–free emission map was required (Planck Collaboration et al. 2016). To convert the emission map into a free–free intensity map, the conversion factor is $I_{\nu} = 46.04 \text{ Jy sr}^{-1}$ at 353 GHz (from Finkbeiner 2003) was applied. Equation (5) from Sodroski et al. (1997) is then used to derive the HII column density. Here, we use an effective electron density (n_{eff}) of 10 cm^{-3} as a lower limit. Similarly to the Planck hydrogen column density, the HII column density is integrated along the whole line of sight. The bottom panel of Figure F.6 shows the ratio

between column density derived from the dust opacity map and column density from free-free emission (HII column density).

The total hydrogen column density traced by the HI and ^{12}CO emission is taken along the entire line of sight ($v_{\text{lsr}} = 50$ to 150 km s^{-1}) to allow for comparison between it and the Planck data, which has no distance information.

The total hydrogen column density (top panel of Figure F.6) has morphological similarities to the total column density as derived from the dust opacity map, as demonstrated in the middle panel of Figure F.6. In particular, we note the dense region of gas to the Galactic South of the TeV source present in both column density maps. They are also on the same order of magnitude; hence to compare the HII column density with the total hydrogen column density, it is acceptable to use the dust opacity column density. This ratio is presented in the bottom panel of Figure F.6. The ratio values indicate that the total neutral column density is dominating over the component of ionised gas. For this purpose, the total column density used throughout this paper does not take the ionised gas into account.

F.1. Dense gas tracer mosaics

Table F.1 shows the molecular lines that were observed by the 7-mm observing set-up for the MOPS.

The integrated intensity maps for the various dense gas tracers towards HESS J1804–216 are presented in Figure F.7, F.8, F.9, F.10 and F.11.

SiO(1-0, $v = 0$) emission has been detected towards HESS J1804–216; however, it is quite weak. There are a few dense features in components B, C, and D; however, these show features which have already been seen in the other dense gas tracers (see Section 4.2).

In Figure F.11, we have included the known H₂O maser positions from Walsh *et al.* (2011), at their given velocities.

G. CR spectra model

Equation (7) can be adjusted to calculate the CR enhancement factor from the GeV γ -rays from FGES J1804.8–2144, as shown by Equation (G.1). An integral power law spectrum of $E^{-1.75}$ is assumed, following Aharonian (1991) for GeV energies:

$$F(\geq E_\gamma) = 1.45 \times 10^{-13} E_{\text{TeV}}^{-1.75} \left(\frac{M_5}{d_{\text{kpc}}^2} \right) k_{\text{CR}} \text{ cm}^{-2} \text{ s}^{-1}, \quad (\text{G.1})$$

The photon flux for γ -rays from FGES J1804.8–2144 is $F(\geq 10 \text{ GeV}) = 1.56 \times 10^{-9} \text{ cm}^{-2} \text{ s}^{-1}$ (Ackermann *et al.* 2017). This leads to a CR enhancement factor, k_{CR} , of ~ 9 times that of the Earth-like CR density for SNR G8.7–0.1 (component D) at GeV energies.

Using Equation (14), the energy spectrum of CR protons is obtained for a range of diffusion suppression factors, χ 's, and indices of the diffusion coefficient, δ 's, to test the validity of each value, as shown in Figure G.1.

Values of $\delta = 0.5$ & 0.7 for $\chi = 0.01$ are the most plausible for the hadronic scenario for SNR G8.7–0.1 (see Section 5.1).

Figure G.2 shows the energy spectrum of CR protons escaping from the progenitor SNR of PSR J1803–2137. The total energy budget of CRs in this scenario is taken to be 10^{48} erg which is consistent with $W_{p,\text{TeV}}$ from Equation (5) (see also Table 3) using component C. A CR enhancement factor, k_{CR} , of ~ 57 is obtained for TeV energies (using Equation (7)) and ~ 14 for GeV energies (using Equation (G.1)).

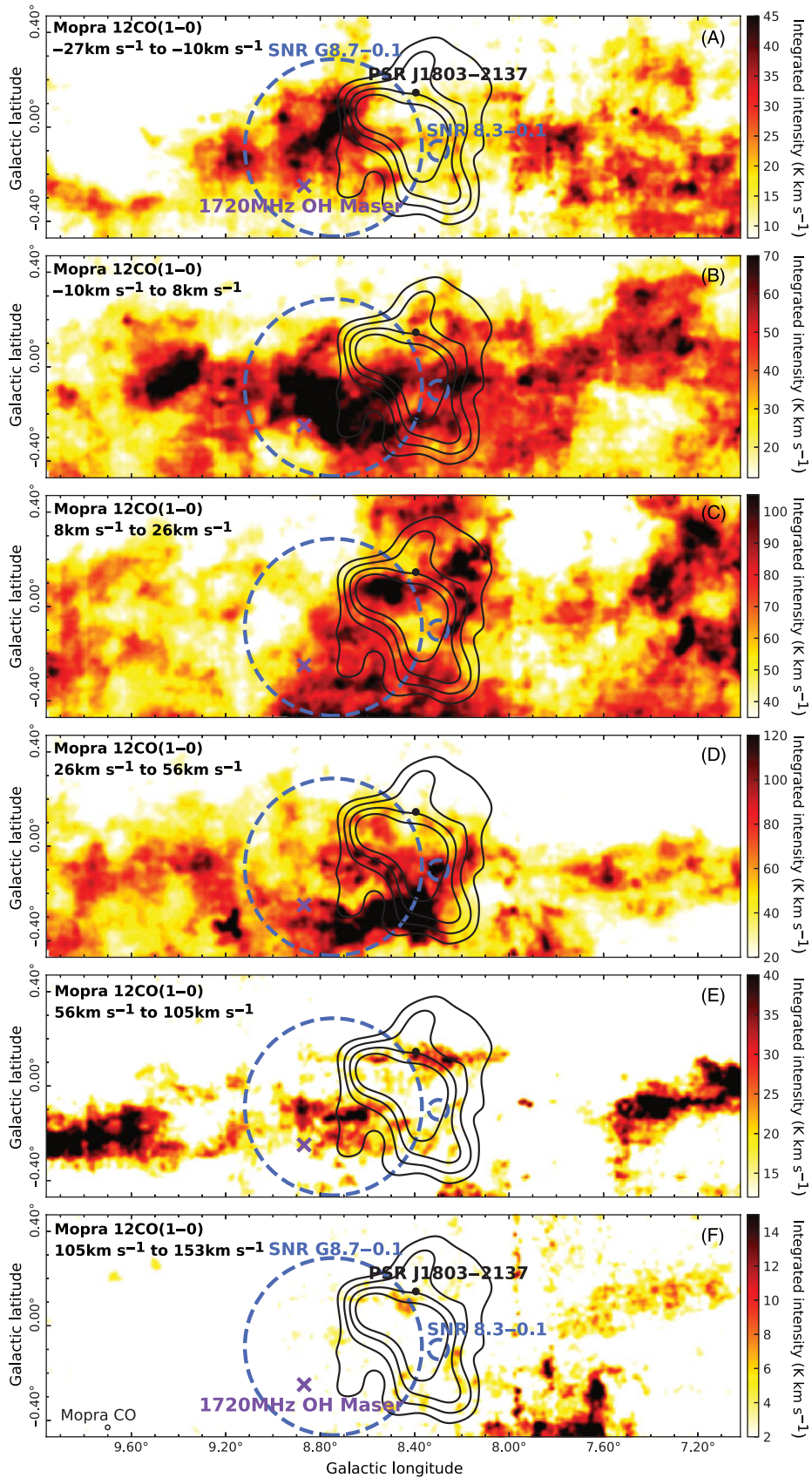


Figure F.1. Mosaic of Mopra $^{12}\text{CO}(1-0)$ integrated intensity maps (K km s^{-1}) towards HESS J1804–216, for gas components A–F as defined in Figure 2. The two dashed blue circles indicate SNR G8.7–0.1 and SNR 8.3–0.1. The 1720-MHz OH is indicated by the purple cross and PSR J1803–2137 is indicated by the black dot. The TeV γ -ray emission for $5-10\sigma$ is shown by the solid black contours.

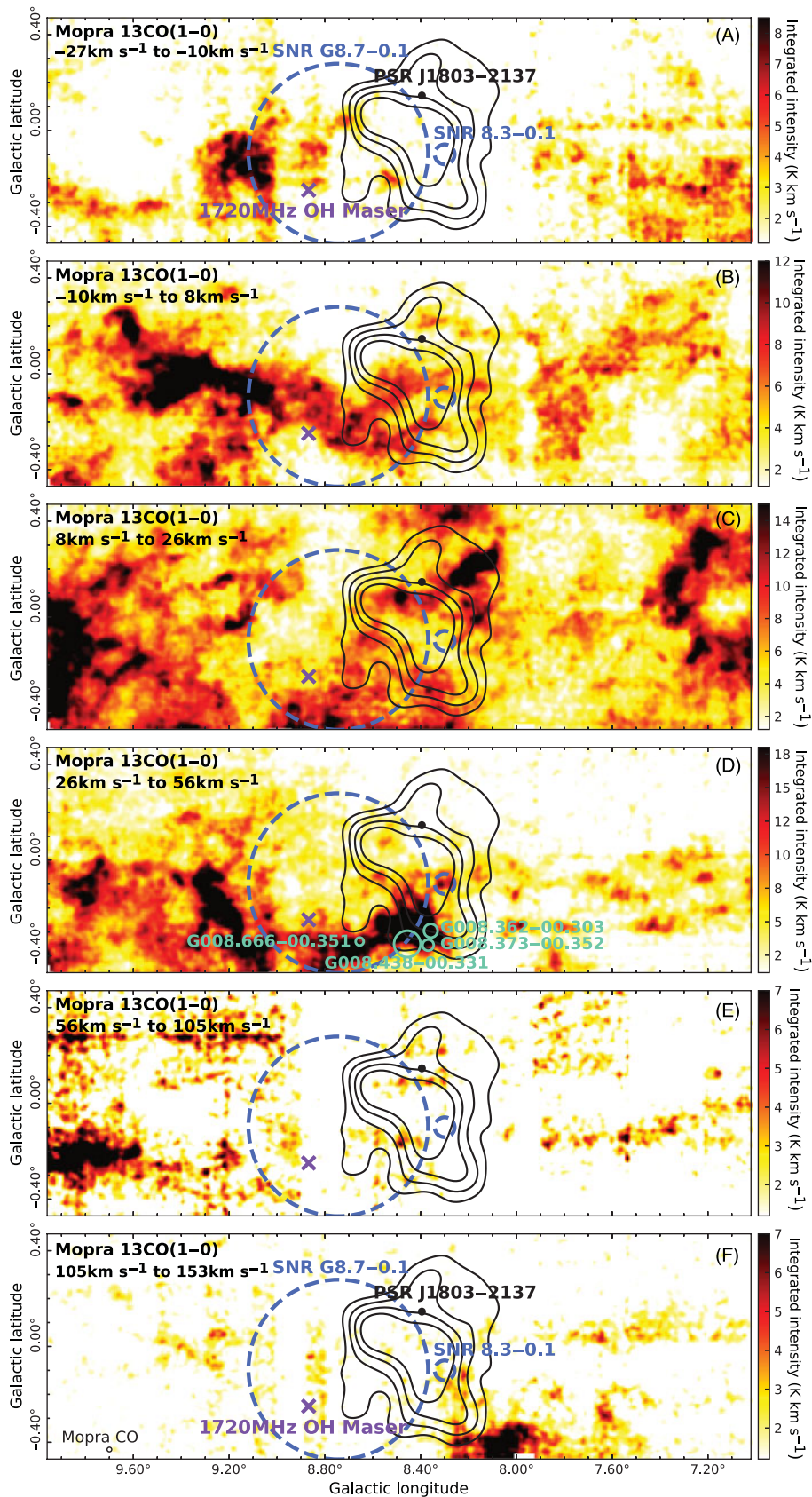


Figure F.2. Mosaic of Mopra ^{13}CO integrated intensity maps (K km s^{-1}) towards HESS J1804–216. The two dashed blue circles indicate SNR G8.7–0.1 and SNR 8.3–0.1. The 1720-MHz OH is indicated by the purple cross and PSR J1803–2137 is indicated by the black dot. The TeV γ -ray emission for $5-10\sigma$ is shown by the solid black contours. The aqua circles in component D indicate HII regions.

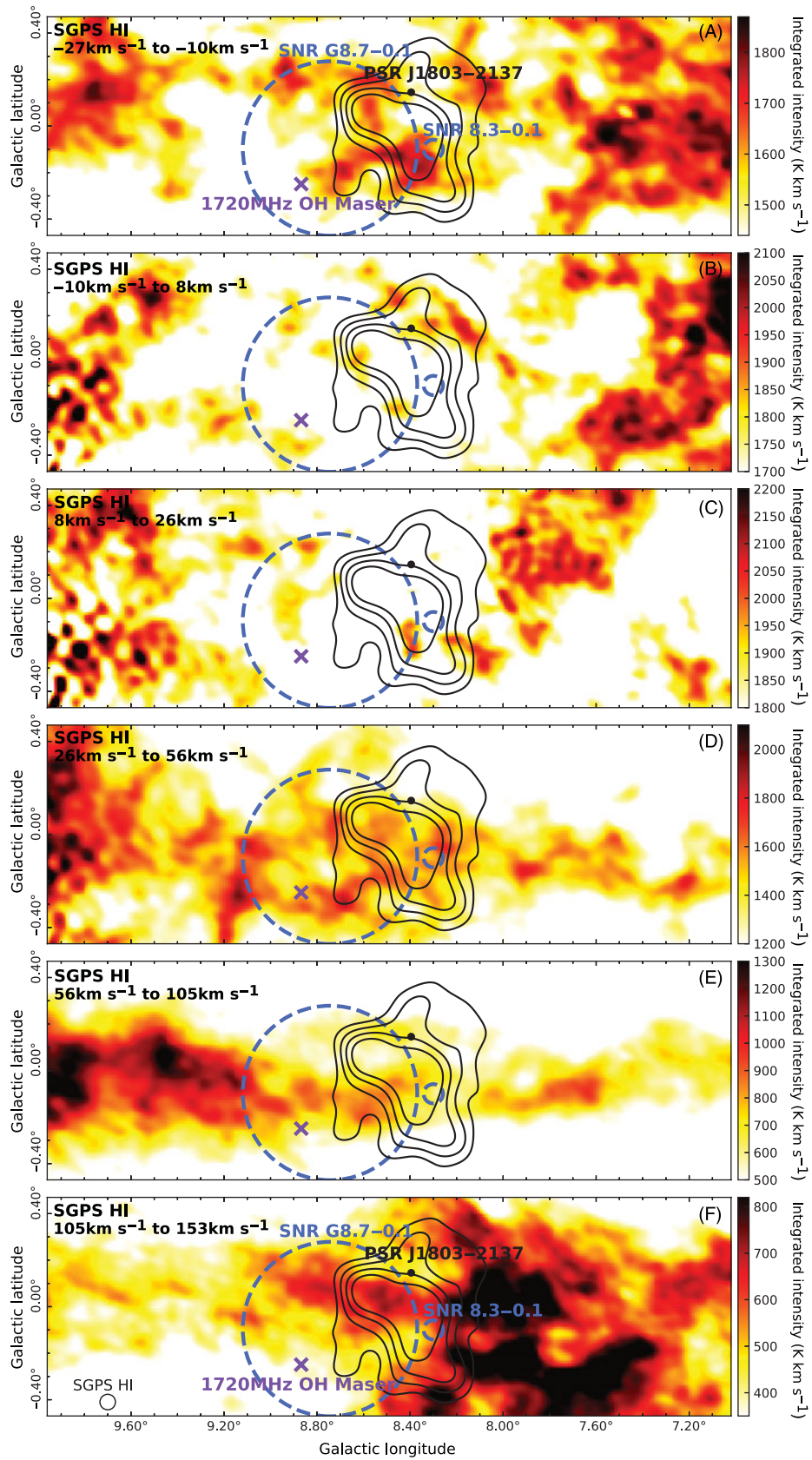


Figure F.3. Mosaic of SGPS HI integrated intensity maps (K km s^{-1}) towards HESS J1804–216. The two dashed blue circles indicate SNR G8.7–0.1 and SNR 8.3–0.1. The 1720-MHz OH is indicated by the purple cross and PSR J1803–2137 is indicated by the black dot. The TeV γ -ray emission for $5\text{-}10\sigma$ is shown by the solid black contours.

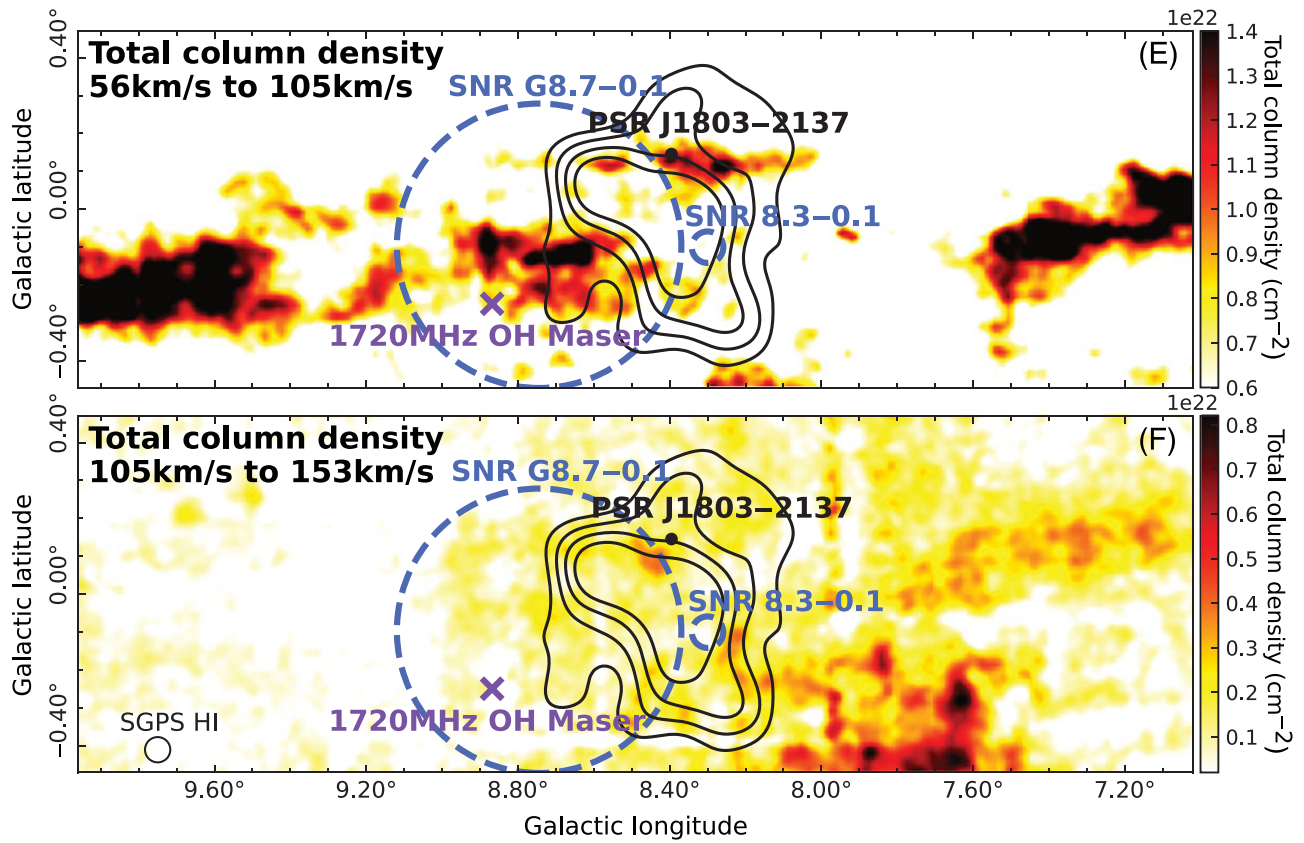


Figure F.4. Total column density maps, $2N_{\text{H}_2} + N_{\text{HI}}$, (cm^{-2}) towards HESS J1804–216, for gas components E and F. The two dashed blue circles indicate SNR G8.7–0.1 and SNR 8.3–0.1. The 1720-MHz OH is indicated by the purple cross and PSR J1803–2137 is indicated by the black dot. The TeV γ -ray emission for $5\text{-}10\sigma$ is shown by the solid black contours.

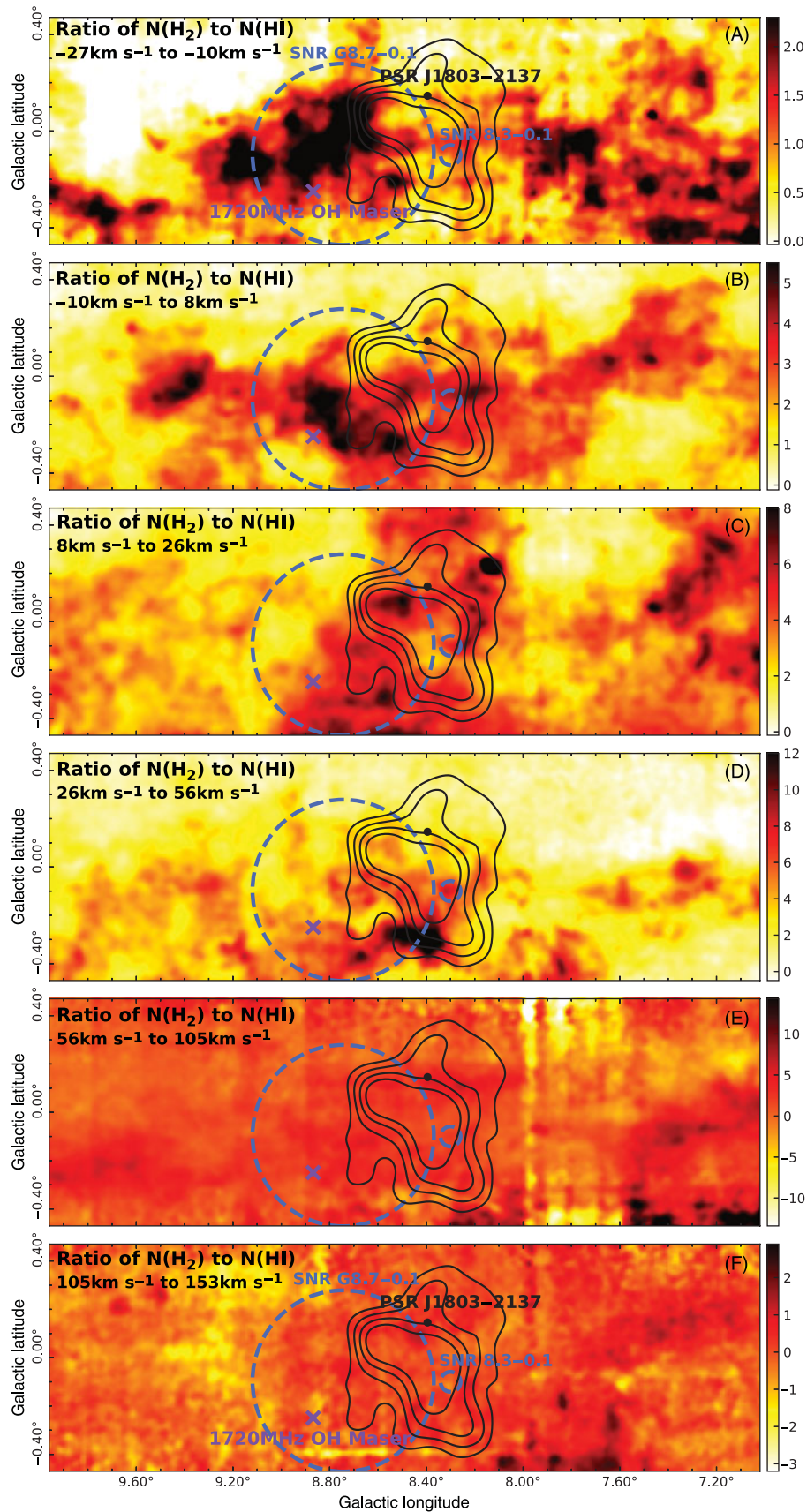


Figure F.5. Ratio of molecular hydrogen ($N(\text{H}_2)$) and atomic hydrogen ($N(\text{HI})$) column densities towards HESS J1804–216, for gas components A–E. The two dashed blue circles indicate SNR G8.7–0.1 and SNR 8.3–0.1. The 1720-MHz OH is indicated by the purple cross and PSR J1803–2137 is indicated by the black dot. The TeV γ -ray emission for $5-10\sigma$ is shown by the solid black contours.

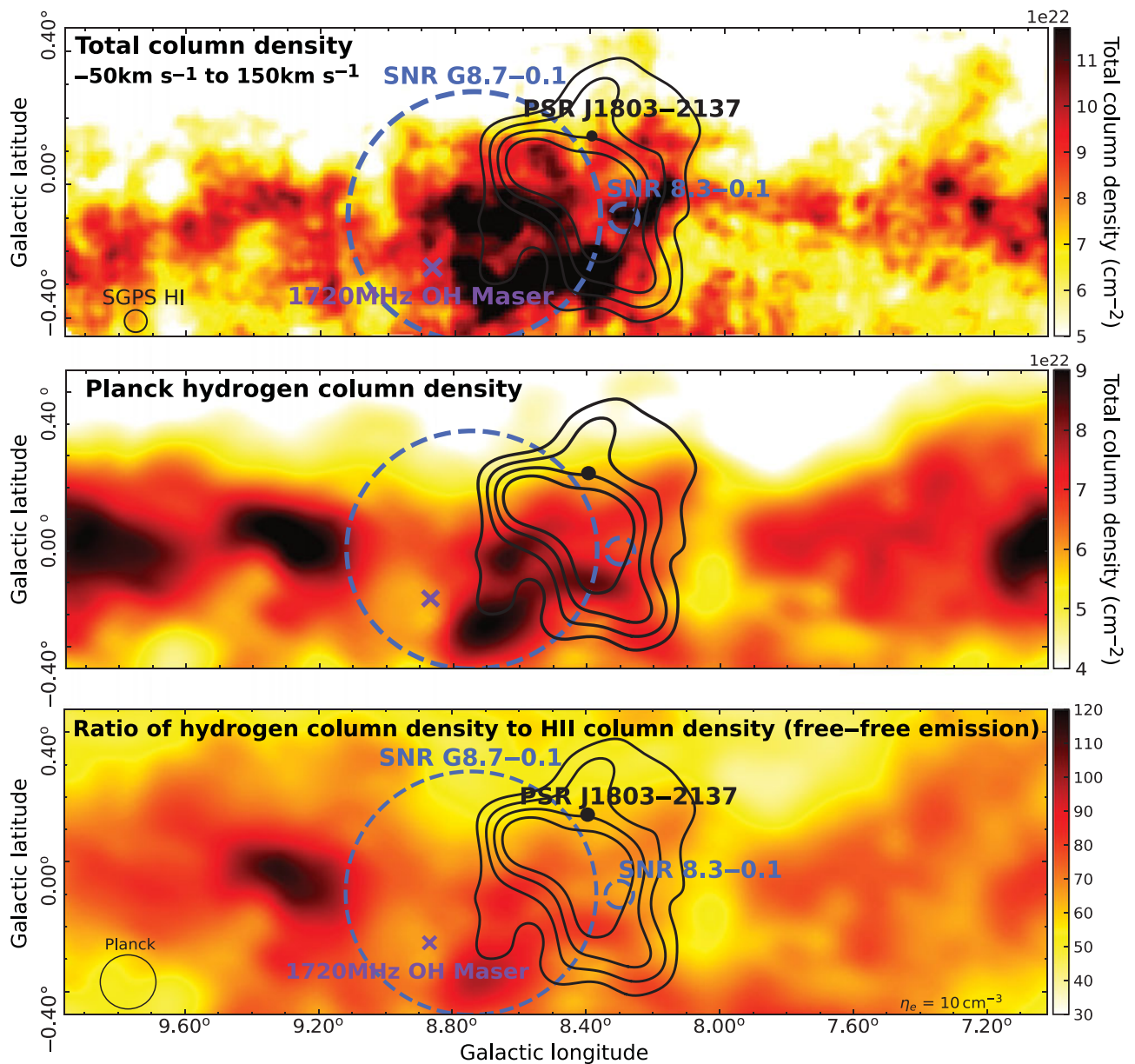


Figure F.6. *Top:* Total column density map (cm^{-2}) from the SGPS HI and Mopra ^{12}CO emission, along the entire line of sight ($v_{\text{lsr}} = 50$ to 150 km s^{-1}) of HESS J1804–216. *Middle:* Planck hydrogen column density. *Bottom:* Ratio of hydrogen column density as derived from Planck dust opacity and HII column density from free-free emission. *All:* The two dashed blue circles indicate SNR G8.7–0.1 and SNR 8.3–0.1. The 1720-MHz OH is indicated by the purple cross and PSR J1803–2137 is indicated by the black dot. The TeV γ -ray emission for $5-10\sigma$ is shown by the solid black contours.

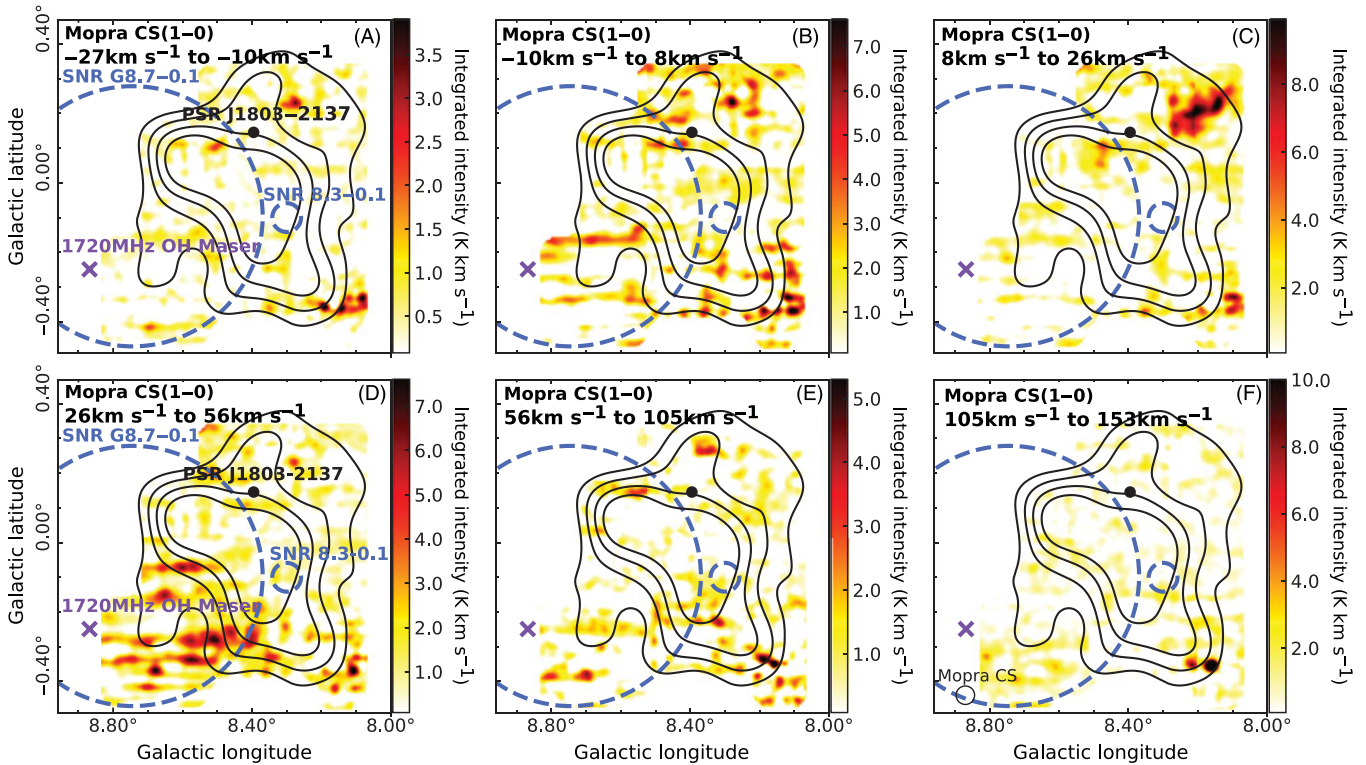


Figure F.7. CS(1-0) integrated intensity maps (K km s⁻¹) towards HESS J1804–216. For components A through F, the T_{rms} is 2.5, 2.7, 2.8, 3.5, 4.3, and 4.2 K, respectively. The two dashed blue circles indicate SNR G8.7–0.1 and SNR 8.3–0.1. The 1720-MHz OH is indicated by the purple cross and PSR J1803–2137 is indicated by the black dot. The TeV γ -ray emission for 5-10 σ is shown by the solid black contours.

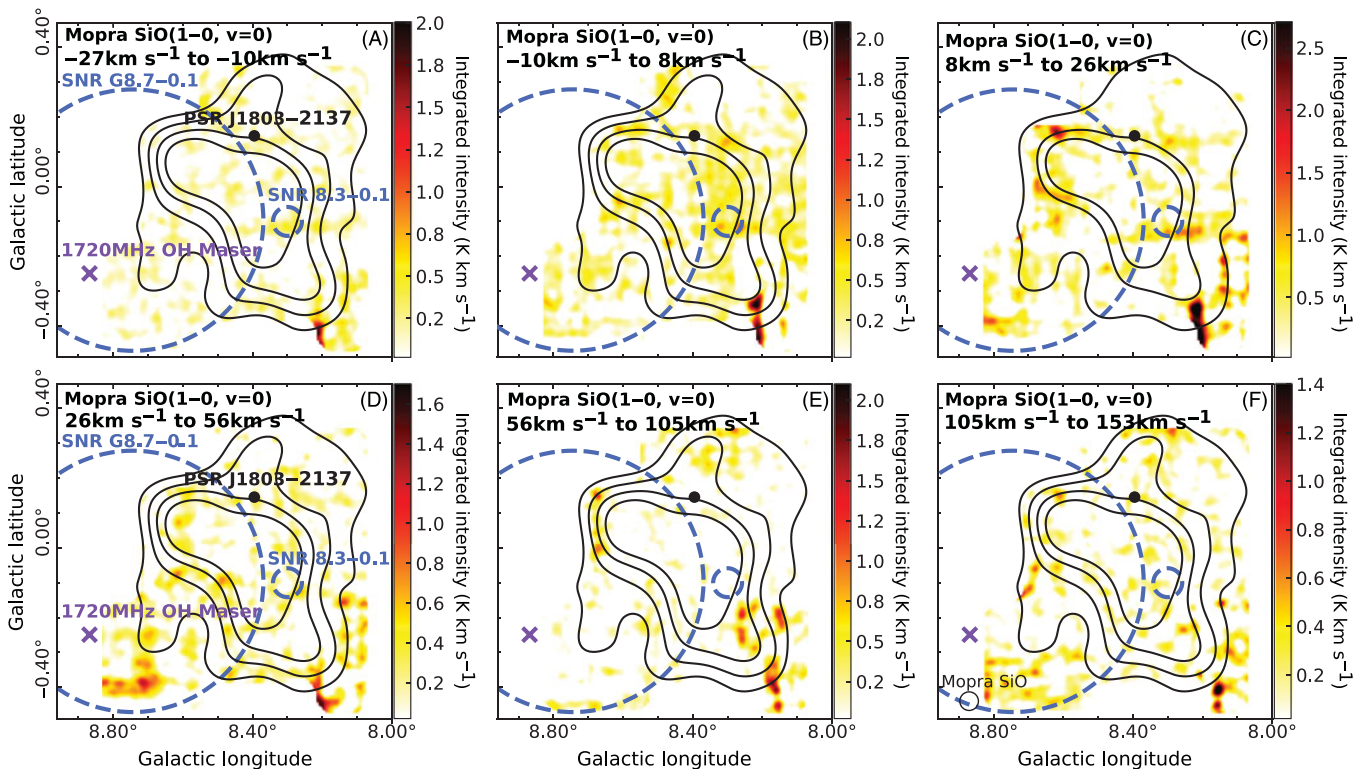


Figure F.8. SiO(1-0, $v = 0$) integrated intensity maps (K km s⁻¹) towards HESS J1804–216. For components A through F, the T_{rms} is 1.3 K, 1.3 K, 1.4 K, 1.7 K, 2.2 K, and 2.2 K, respectively. The two dashed blue circles indicate SNR G8.7–0.1 and SNR 8.3–0.1. The 1720-MHz OH is indicated by the purple cross and PSR J1803–2137 is indicated by the black dot. The TeV γ -ray emission for 5-10 σ is shown by the solid black contours.

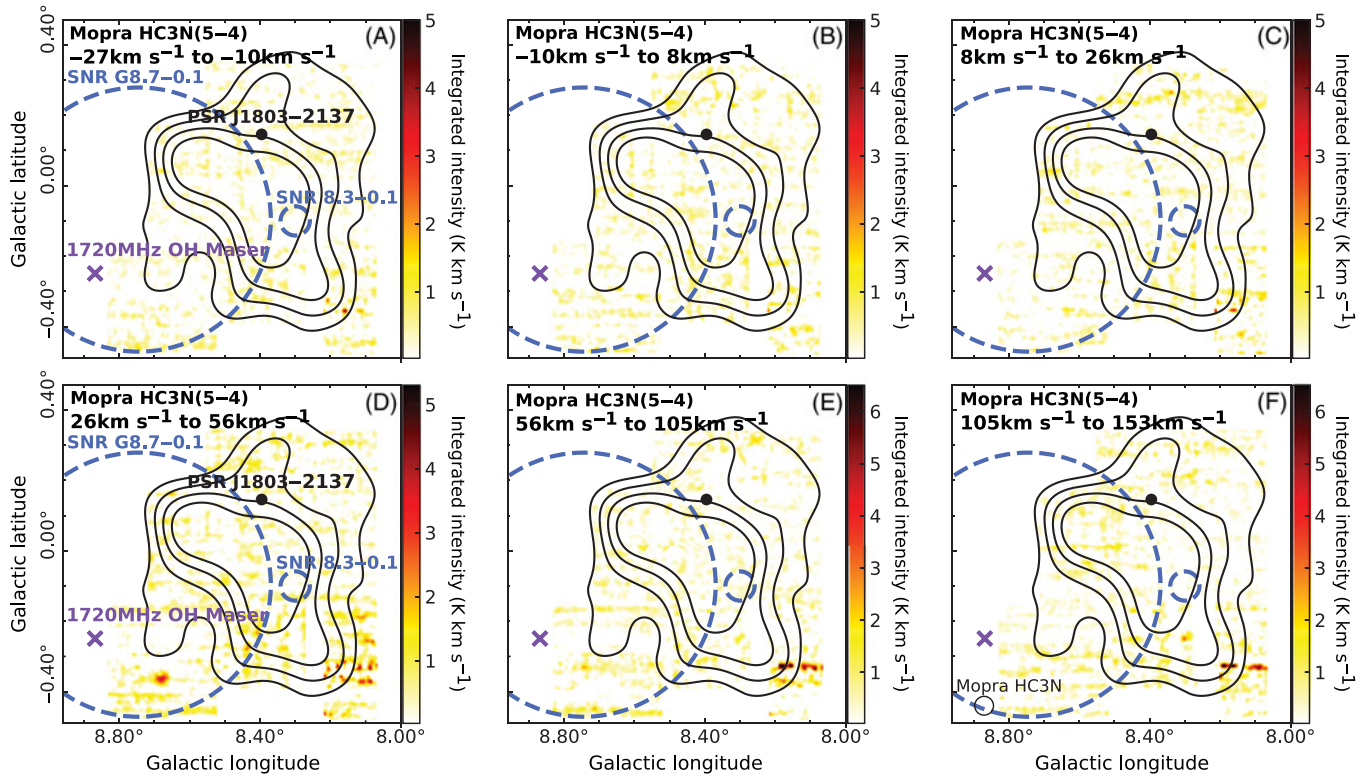


Figure 9. HC₃N(5-4) integrated intensity maps (K km s^{-1}) towards HESS J1804–216. For components A through F, the T_{rms} is 3.6 K, 3.8 K, 3.8 K, 4.9 K, 6.1 K, and 6.1 K, respectively. The two dashed blue circles indicate SNR $8.7-0.1$ and SNR $8.3-0.1$. The 1720-MHz OH is indicated by the purple cross and PSR J1803–2137 is indicated by the black dot. The TeV γ -ray emission for $5-10\sigma$ is shown by the solid black contours.

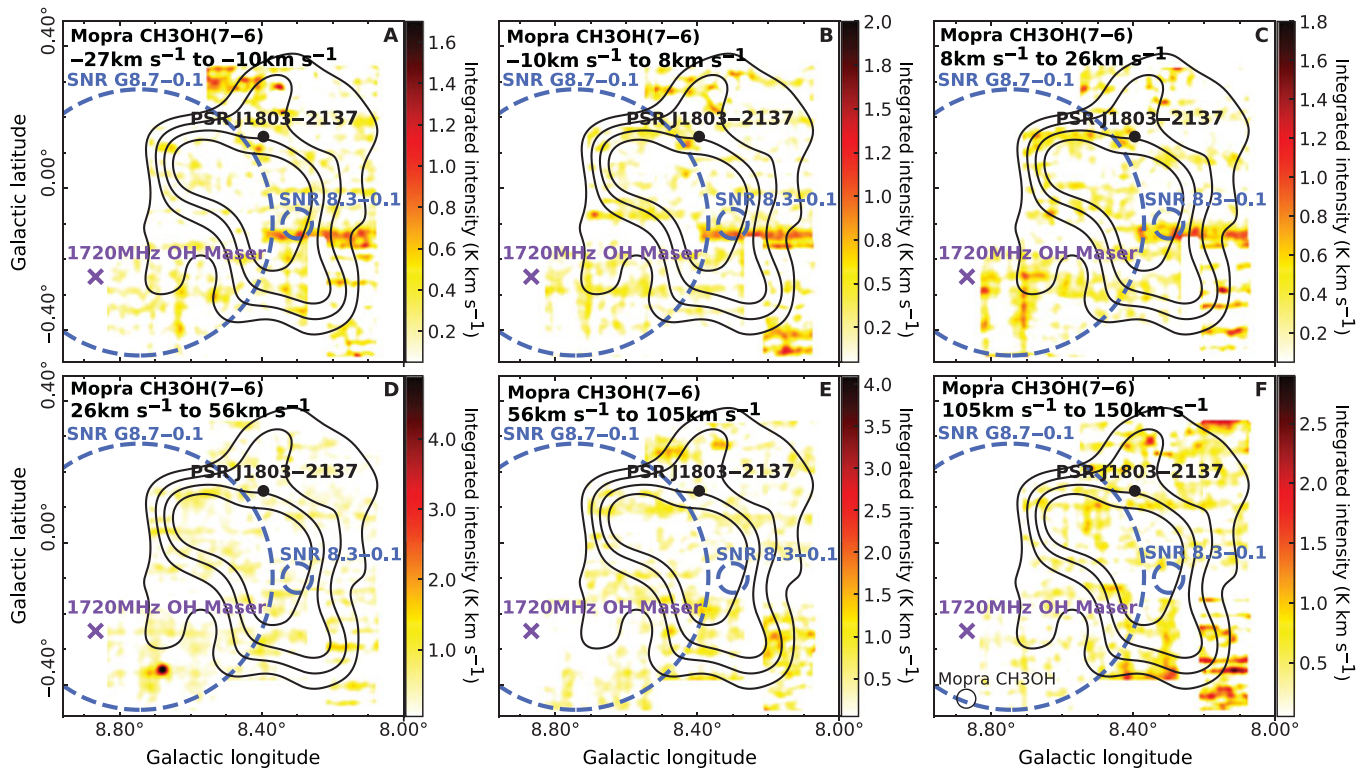


Figure 10. CH₃OH(7-6) integrated intensity maps (K km s^{-1} , uncleaned) towards HESS J1804–216. For components A through F, the T_{rms} is 0.8 K, 0.9 K, 0.9 K, 1.1 K, 1.4 K, and 1.4 K, respectively. The two dashed blue circles indicate SNR $8.7-0.1$ and SNR $8.3-0.1$. The 1720-MHz OH is indicated by the purple cross and PSR J1803–2137 is indicated by the black dot. The TeV γ -ray emission for $5-10\sigma$ is shown by the solid black contours.

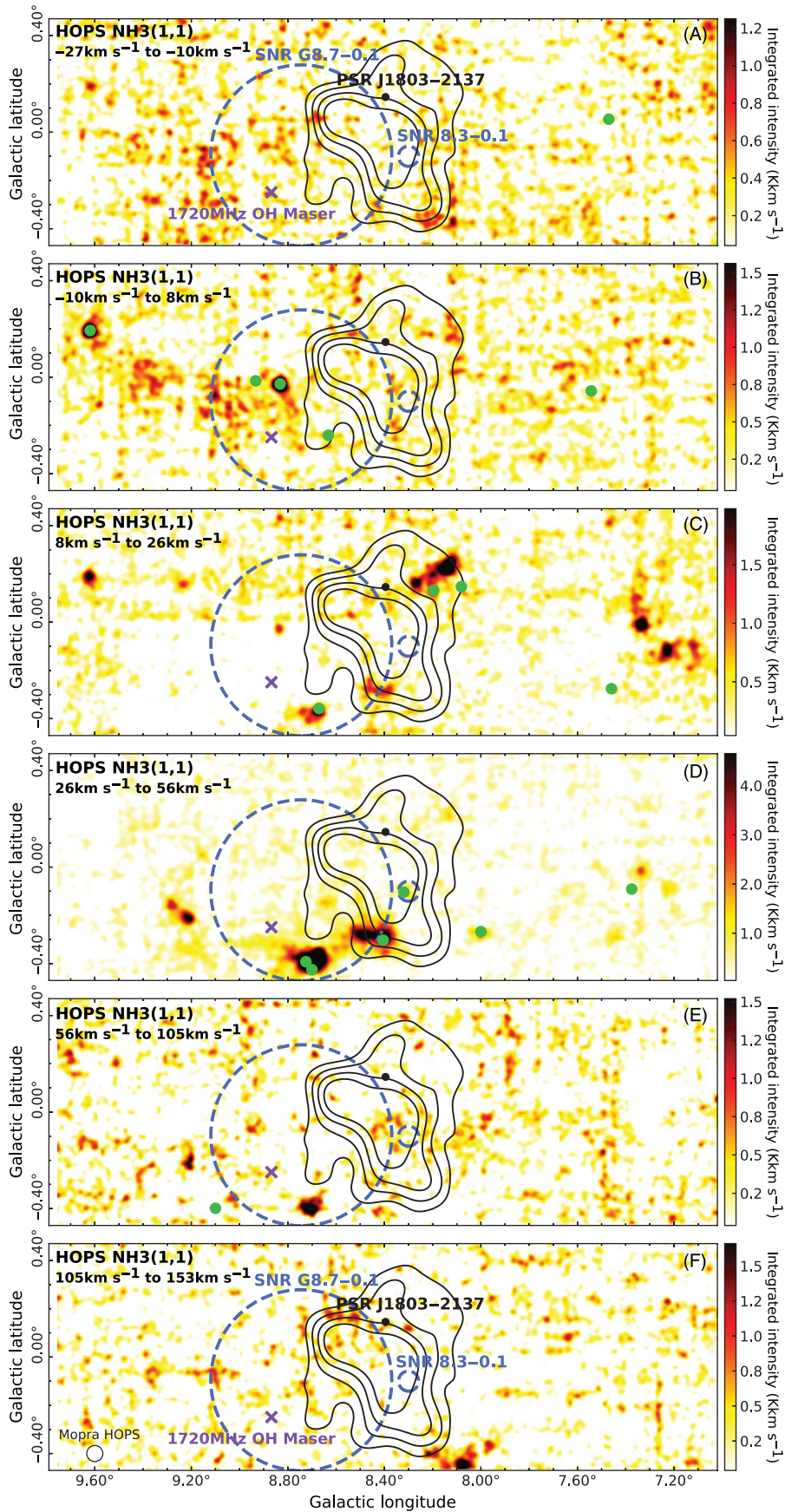


Figure F.11. $\text{NH}_3(1,1)$ integrated intensity maps (K km s⁻¹) towards HESS J1804-216 using HOPS data. The two dashed blue circles indicate SNR G8.7-0.1 and SNR 8.3-0.1. The 1720-MHz OH is indicated by the purple cross and PSR J1803-2137 is indicated by the black dot. The TeV γ -ray emission for 5-10 σ is shown by the solid black contours. H₂O maser positions are shown by the green dots.

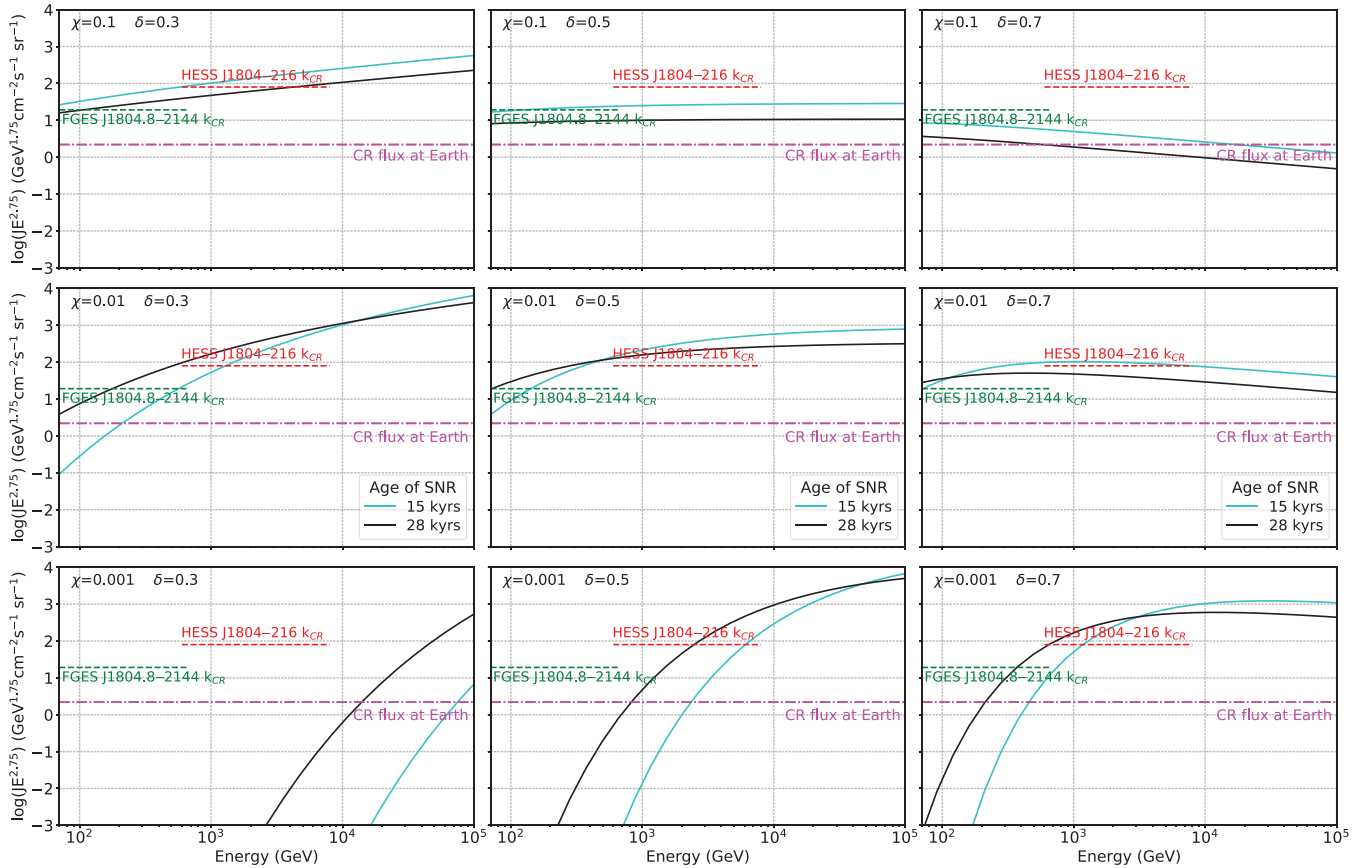


Figure G.1. Modelled energy spectra of CR protons (Equation (14)) escaping from the potential impulsive accelerator SNR G8.7–0.1, with a total energy of 2×10^{48} erg in CRs. Various values of diffusion suppression factor, χ , and index of the diffusion coefficient, δ , are shown here. A power law spectrum with a spectral index of $\alpha = 2$ is assumed. The number density is taken to be $n = 160 \text{ cm}^{-3}$. The distance from the accelerator to the cloud is $R \sim 12 \text{ pc}$ and age of the source are taken to be 15 kyr and 28 kyr for the cyan and black curves, respectively. The magenta dashed line represents the CR flux observed at Earth. The red represents the calculated CR enhancement factor for HESS J1804–216 ($k_{CR} \approx 37$). The green represents the calculated CR enhancement factor for FGES J1804.8–2144 ($k_{CR} \approx 9$).

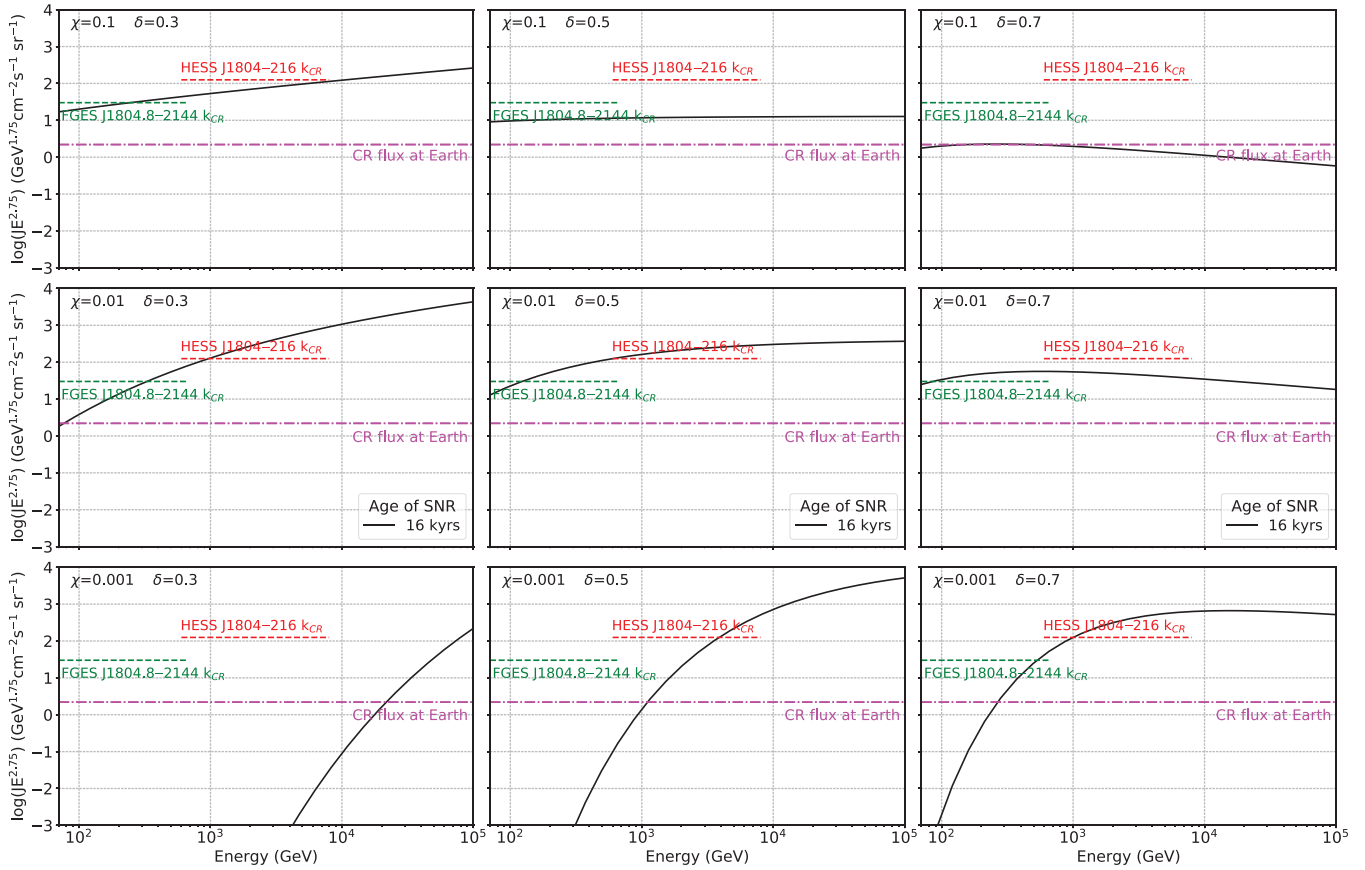


Figure G.2. Modelled energy spectra of CR protons (Equation (14)) escaping from the potential impulsive accelerator (progenitor SNR from PSR J1803–2137), with a total energy of 10^{48} erg in CRs. Various values of diffusion suppression factor, χ , and index of the diffusion coefficient, δ , are shown here. A power law spectrum with a spectral index of $\alpha = 2$ is assumed. The number density is taken to be $n = 325 \text{ cm}^{-3}$. The distance from the accelerator to the cloud is $R \sim 10 \text{ pc}$ and age of the source is taken to be 16 kyr for the black curves. The magenta dashed line represents the CR flux observed at Earth. The red represents the calculated CR enhancement factor for HESS J1804–216 ($k_{CR} \approx 57$). The green represents the calculated CR enhancement factor for FGES J1804.8–2144 ($k_{CR} \approx 14$).